

Research Article

# Quartz Vein Formation and Deformation during Porphyry Cu Deposit Formation: A Microstructural and Geochemical Analysis of the Butte, Montana, Ore Deposit

Marisa D. Acosta<sup>1</sup>, Mark H. Reed,<sup>2</sup> and James M. Watkins<sup>2</sup>

<sup>1</sup>Institute of Earth Sciences, University of Lausanne, Géopolis, Lausanne, Vaud, Switzerland CH-1015

<sup>2</sup>Department of Earth Sciences, University of Oregon, 1272 E 13th Ave., Eugene, OR 97403, USA

Correspondence should be addressed to Marisa D. Acosta; [macosta@uoregon.edu](mailto:macosta@uoregon.edu)

Received 25 February 2022; Accepted 28 July 2022; Published 24 August 2022

Academic Editor: Feng Cheng

Copyright © 2022 Marisa D. Acosta et al. Exclusive Licensee GeoScienceWorld. Distributed under a Creative Commons Attribution License (CC BY 4.0).

Hydrothermal quartz veins from the Butte deposit display euhedral and mottled cathodoluminescent (CL) textures that reflect the growth and deformation history of quartz crystals. A CL-euhedral texture consists of oscillatory dark-light zonations that record primary precipitation from an aqueous fluid. The origin of a CL-mottled texture, which consists of irregularly distributed dark and light portions, is less clear. Previous work showed that in some veins, CL-euhedral and CL-mottled crystals coexist, but the processes leading to their formation and coexistence were unknown. We find that CL-mottled crystals occur predominantly along the wall rock fracture surface and in vein centers and that CL-euhedral cockscomb quartz protrudes from the mottled layers along the wall rock. We infer that the mottled crystals formed by strain-induced recrystallization that was preferentially accommodated by the rheologically weaker layers of noncockscomb quartz because cockscomb crystals are in hard glide orientations relative to adjacent noncockscomb layers. During strain, crystals in noncockscomb layers that are not initially susceptible to slip can rotate in their deforming matrix until they deform plastically. Some of the CL-mottled crystals exhibit a relict CL-euhedral texture ("ghost bands") whereby bright bands have been blurred and deformed owing to Ti redistribution facilitated by grain boundary migration. The edges of some CL-euhedral crystals become CL-mottled by localized grain boundary migration along adjacent crystals that do not align perfectly. Throughout the veins, CL-mottled crystals are randomly oriented, indicating that small deviatoric stresses were sufficient to drive recrystallization and mobilization of trace elements. Ti concentrations in CL-mottled crystals (23-47 ppm Ti; mean of 31 ppm) overlap those of CL-euhedral dark growth bands (16-40 ppm Ti; mean of 25 ppm Ti) in neighboring CL-euhedral crystals. Average Ti concentrations in CL-mottled quartz and CL-euhedral dark growth bands correspond to temperature estimates of 600°C (31 ppm Ti; CL-mottled) and 619°C (25 ppm Ti; dark bands), which are in good agreement with previous quartz precipitation temperature estimates based on independent thermobarometers. We conclude that recrystallization resets CL-mottled Ti concentrations close to the equilibrium value for the conditions of deformation and that CL-dark growth bands record near-equilibrium Ti concentrations. Recognition of widespread quartz recrystallization in porphyry Cu deposits underscores the significant role that strain plays in deposit formation. Individual veins host crystals that preserve conditions of primary growth and other crystals that preserve conditions of deformation and thermal overprint. Textural information is key to accurately interpreting trace element data and identifying different stages of vein formation. Our suggestion that CL-dark bands are the best candidates for near-equilibrium growth will aid the interpretation of trace element zoning in other hydrothermal systems.

## 1. Introduction

Quartz vein stockworks in porphyry copper deposits form when overpressurized fluid above a crystallizing magma

chamber invades the country rock and precipitates minerals in the fractures. The mineral content of veins and adjacent alteration envelopes changes through time as the fluids decompress and cool from near-magmatic temperature

(~700°C) in the early stages to 350°C and below [1]. The existing large body of work on quartz vein microstructures in metamorphic rocks ([2] and references therein) forms a starting point for this work on high temperature quartz deformation in porphyry Cu deposits and the connection of quartz deformation microstructures to vein formation. In this contribution, we combine scanning electron microscope-cathodoluminescence (CL) imaging with electron backscatter diffraction (EBSD) to show that high temperature quartz veins in the Butte porphyry Cu-Mo deposit contain oriented undeformed euhedral crystals juxtaposed with randomly oriented deformed quartz grains that recrystallized by grain boundary migration and that recrystallization occurred at roughly the same temperature as the initial quartz precipitation.

Butte veins display three metamorphic quartz recrystallization regimes: bulging recrystallization, subgrain rotation, and grain boundary migration [3, 4]. Each regime creates characteristic microstructures that occur in different parts of the Butte vein system, though grain boundary migration is by far the most abundant. The various recrystallization microstructures correlate to different recrystallization temperatures and to deformation at different strain rates and magnitudes, as described herein.

The 65 Ma Butte porphyry Cu-Mo deposit provides an ideal study site because it has been thoroughly studied for more than 100 years [5] and because it is hosted by the homogeneous Butte Granite (Figure 1(a)) [6, 7], which eliminates geochemical and structural complexities caused by heterogeneous country rock. The veins and vein envelopes are well-characterized at Butte, as explained below, but some key observations lack explanation. Earlier investigations into barren quartz/quartz-molybdenite veins revealed two cathodoluminescence (CL) textures [8–10], hereafter referred to as “CL-euhedral” and “CL-mottled.” CL-euhedral texture consists of alternating dark and light growth zones of euhedral crystal faces, reflecting primary crystal growth from a hydrothermal fluid (Figure 2(a)). CL-mottled crystals are unevenly dappled with patches of darker CL on a background of lighter CL (Figure 2(c)). A third texture consists of wavy concentric “ghost” bands (Figure 2(b)). While CL-euhedral textures reflect crystal growth zoning, the origin of CL-mottled and ghost bands texture has been puzzling. In quartz-molybdenite veins, CL-mottled quartz is contiguous with CL-euhedral quartz. Crystals in deep barren quartz veins from drill holes that intersected the cupola region of the Butte deposit are exclusively CL-mottled. We present evidence that CL-mottled crystals form by grain boundary migration in CL-euhedral crystals and suggest that coexistence of the two textures is a consequence of preferential deformation in vein centers shortly after vein formation. We interpret the intermediate ghost band texture as relict CL-euhedral crystals that partially recrystallized, but strain ceased before the texture ripened to mottled. We argue that the preponderance of CL-mottled crystals in barren quartz veins is the result of extensive episodic deformation near the base of the deposit, directly above the magma body that underlies the magmatic cupola.

## 2. Geologic Background

The Butte porphyry Cu-Mo ore deposit is hosted in the 76 Ma Butte Granite [11]. The Butte Granite intruded the Proterozoic Belt Supergroup, a marine sedimentary sequence, and Archean crystalline basement to the south of Butte [5]. The granitic melt likely formed when the Paleo-proterozoic basement was partially melted by and mixed with mantle-derived melts when subduction in North America was happening at a low angle in the Late Cretaceous [11]. Emplacement of the Butte Granite into the cogenetic Elkhorn Mountain Volcanics was structurally controlled by reactivated Precambrian faults, which also controlled the emplacement of other intrusive members of the Boulder Batholith [12, 13] and occurred when the region was experiencing compression with the maximum compressive stress-oriented east-west. Based on geophysical data, Berger et al. [12] identified a southern feeder zone for the Butte Granite, whose structures also served to focus mineralizing fluids. Within the Butte Granite are alaskite and granoaplite dikes and sills that are the products of late high-silica granite crystallization. Following the usage of Roberts [13], alaskite refers to rocks of highly variable textures and grain size that are made up of K-feldspar, albite, and quartz. The term includes aplites, pegmatites, and the gradations between them. Alaskites occur throughout the Boulder batholith as tabular bodies and generally have sharp contacts with the Butte Granite [13]. Alaskites are interpreted as the water-rich residua of the parental Butte Granite melt [13, 14]. Granoaplates are like alaskite but are coarse-grained and porphyritic. Granoaplates have phenocrysts of plagioclase, hornblende, biotite, and quartz eyes set in a groundmass of quartz and alkali feldspar. Contacts between the Butte Granite and granoaplate are gradational.

The Butte deposit consists of early porphyry Cu mineralization known as the pre-Main Stage and subsequent Cordilleran-style base metal veins of the Main Stage. The pre-Main Stage porphyry Cu-Mo ore formed at depths of ~5–9 km [15], and the Main Stage polymetallic veins formed at shallower depths (Figure 1(b)) as fissure fillings in faults [16]. The recently examined genetic link between porphyry deposits and epithermal deposits supports the idea that the Main Stage veins result from the late evolution of the Butte porphyry copper system and are the roots of an epithermal deposit that has been eroded away [17–21].

The Butte system has two concentrically zoned porphyry Cu-Mo domes, distinguished by separate magnetite vein zones and closure of molybdenum grade contours (Figure 1(c)). Each dome is approximately 2 km wide. The western Anaconda dome is separated from the eastern Continental-Pittsmont dome by a bulb-shaped region hosting pyrite veins and pervasive gray sericitic alteration that is 1.2 km wide and extends 2 km deep below the Berkeley Pit (Figure 1(b)).

Pre-Main Stage and Main Stage alteration and mineralization types and relationships have been extensively documented elsewhere [1, 13, 22, 23]. The earliest veins of the potassic series are quartz-chalcopyrite-pyrite veins with biotite, K-feldspar, and sericite alteration envelopes (“EDM”

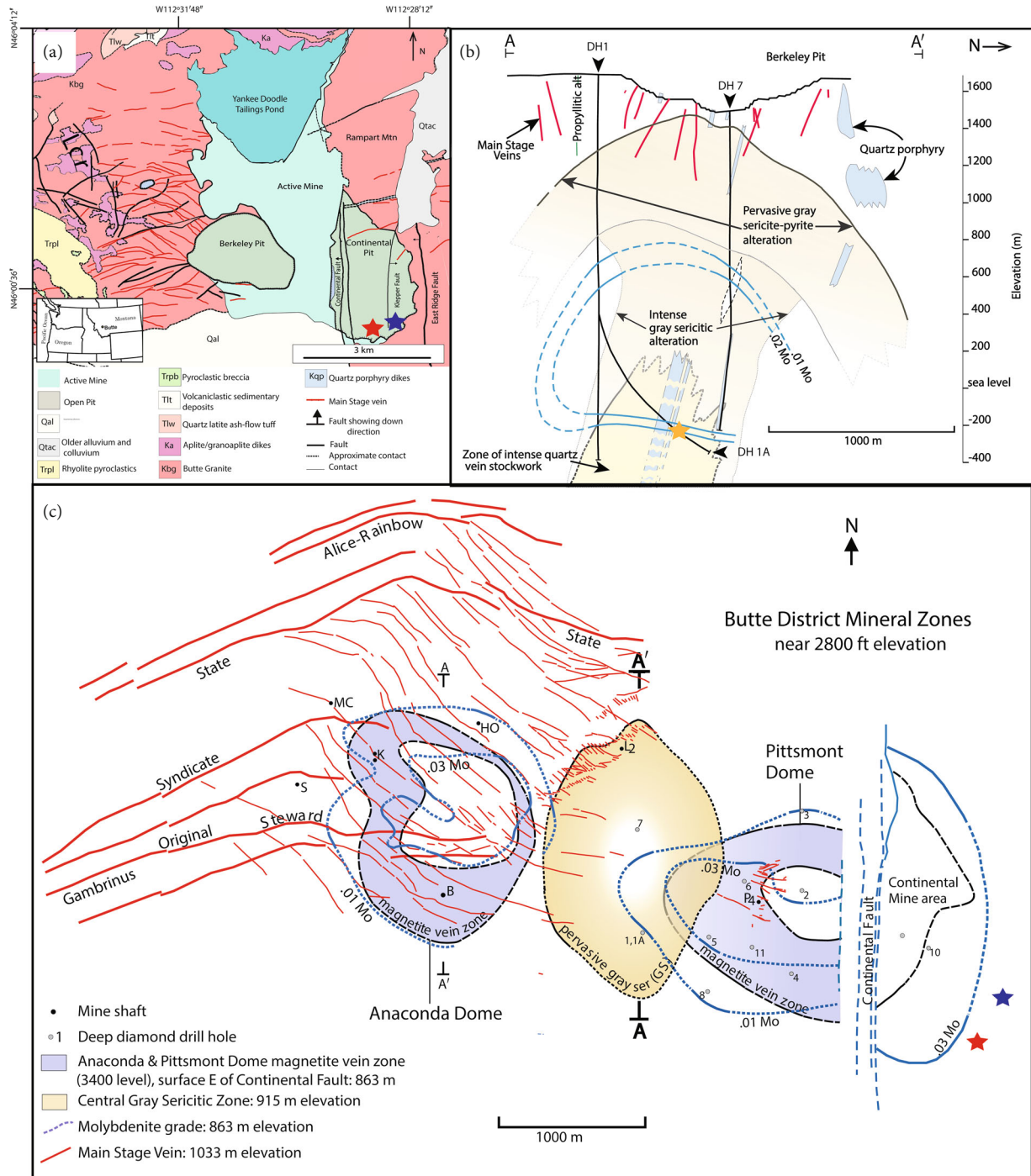


FIGURE 1: The Butte, MT, porphyry Cu-Mo deposit is an active open pit mine situated to the west of the Continental Divide. (a) A simplified geologic map modified from Houston and Dilles (2013). (b) A cross-section through the Central Gray Sericitic Zone from which deep drill core samples that intersected a basal region of intense quartz stockwork were taken. (c) Map of Butte Main Stage veins and pre>Main Stage magnetite vein zones and Mo grades. A-A' shows the location of cross-section in part (b). Mine shafts: B: Belmont; HO: High Ore; K: Kelly; L2: Leonard #2; MC: Mountain Consolidated; P4: Pittsmont #4; S: Steward. There are two porphyry centers separated from one another by a region of gray sericitic alteration. The Pittsmont Dome, the eastern center, is cut by the Continental Fault. (b) and (c) are modified from Reed et al. (2013). Stars indicate approximate sampling locations. The red star is where quartz-molybdenite veins (BMA-018-16Fa and BMA-023-16Fa) were sampled from the Continental Pit in 2014. The blue star is the Main Stage vein, BMA-020-16Fa, which was also sampled from the Continental Pit in 2014. The yellow star is the approximate location where deep barren quartz samples 11052-6121 and 11052-6019 were taken from deep drill hole 1A.

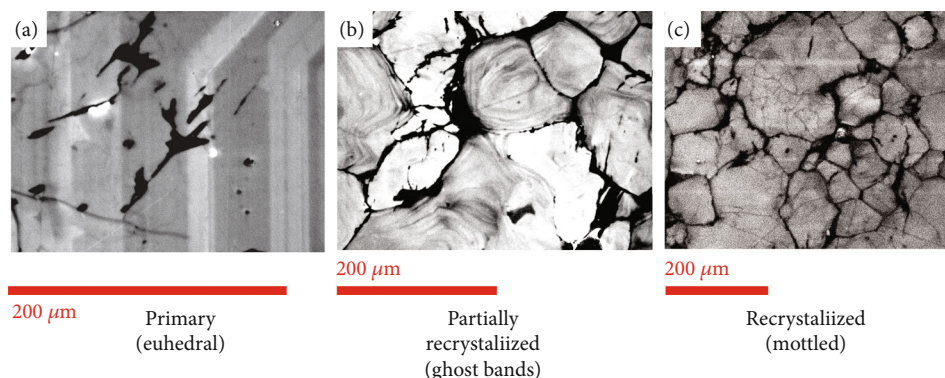


FIGURE 2: The spectrum of growth and deformation CL features observed in high-temperature vein quartz from Butte. (a) CL-euhedral grains are defined by sharp CL brightness boundaries. (b) Partially recrystallized quartz crystals preserve wavy, diffuse remnants of CL-euhedral growth bands. (c) Thoroughly recrystallized quartz is CL-mottled. We interpret the wavy bands as relict CL-euhedral oscillations that were modified by lattice diffusion during grain boundary migration. The CL-black grain boundaries bounding most grains in the mottled and ghost band textured crystals reflect low temperature annealing and fluid-mediated Ti loss.

veins) [22], which include biotite crackles connected to biotite breccias surrounding the apices of quartz porphyry dikes [1]. Biotite crackles are microscopic quartz veinlets with haloes of wall rock altered to biotite, muscovite, and K-feldspar; biotite breccias consist of subangular-subrounded wall rock clasts in a matrix of biotite+quartz+K-feldspar+pyrite [23]. EDM veins vertically grade through a series of alteration types that form because of a single parent fluid cooling and interacting with wall rock at various water-rock ratios [1]. These sulfide-bearing quartz veins are cut by barren quartz and quartz-molybdenite veins. The term “barren” here is a field term that refers to veins with only trace amounts of molybdenite. Barren quartz veins characterize the base of the deposit, forming extensive stockwork zones. Some barren quartz veins grade upwards into quartz-molybdenite veins. The youngest pre-Main Stage veins are pyrite-quartz veins with gray sericitic (GS) alteration in which igneous plagioclase and K-feldspar are replaced by quartz, muscovite, and pyrite and igneous biotite and hornblende are altered to mixtures of muscovite, pyrite, quartz, Mg-chlorite, and rutile [1].

A barren quartz vein stockwork is typical in the root zones of many porphyry Cu-Mo deposits [24, 25] and is accompanied by intense silicification, also known in the literature as “quartz flooding” in the region above the cupola. Intense silicification refers to the addition of large amounts of nonvein quartz to the host rock groundmass, likely by the infiltration of quartz-supersaturated fluids. Barren quartz and quartz-molybdenite veins generally lack alteration envelopes, although thin envelopes containing biotite or K-feldspar occur in the deepest of samples [1]. In this study, we focus on barren quartz from the deep zone of intense silicification intersected by a deep drill hole where quartz-molybdenite veins are nearly absent (sample location shown by the yellow star in Figure 1(b)) and on quartz-molybdenite veins from a shallower region exposed in the Continental Pit where barren quartz veins are rare (sample location shown by the red star in Figure 1(a)). We also describe a quartz-rich Main Stage vein (sample location shown by the blue star in Figure 1(a)). These samples were

chosen because they are representative of the major types of quartz veins in the Butte system and because they represent the spatial and temporal changes in quartz precipitation coeval with deposit formation.

### 3. Methods

Samples are from drill core from deep drill hole 1A (DH-1A, an angled hole that intersected the barren quartz stockwork) and from highwall exposures on the C-East pushback of the Continental Pit. Samples from the pit were collected while mapping the active pit in 2014 in cooperation with Montana Resources. The drill core was sampled during logging of the historic core and is currently housed by Montana Resources at the Montana Bureau of Mines and Geology at Montana Tech. Petrographic descriptions of thick and thin sections were made with an optical microscope. The sections were scanned at high resolution (3200 dpi) in both cross-polarized and plane-polarized light using a Nikon slide scanner. Grain boundary microstructures were identified from thin sections using a petrographic microscope (Figure 3). Representative samples of barren quartz stockwork, quartz-molybdenite veins, and a monogenetic Main Stage vein were analyzed in greater detail using methods described below. All analyses were carried out in the Center for Advanced Materials Characterization in Oregon (CAMCOR) at the University of Oregon, except for electron backscatter diffraction data, which was acquired at the University of Lausanne.

**3.1. SEM-CL.** Thick sections were cleaned with ethanol, coated with ~50 nm of carbon, and imaged with an FEI Quanta 200 FEG environmental scanning electron microscope (SEM) at 15 keV with a beam current of 40 nA. Grayscale cathodoluminescent, secondary electron (SE), and backscattered electron (BSE) images were collected. Major phases were identified using energy dispersive spectroscopy (EDS).

To enable comparisons of the different types of microscopic images we correlated images precisely using Picture-SnapApp (downloadable software from Probe Software,

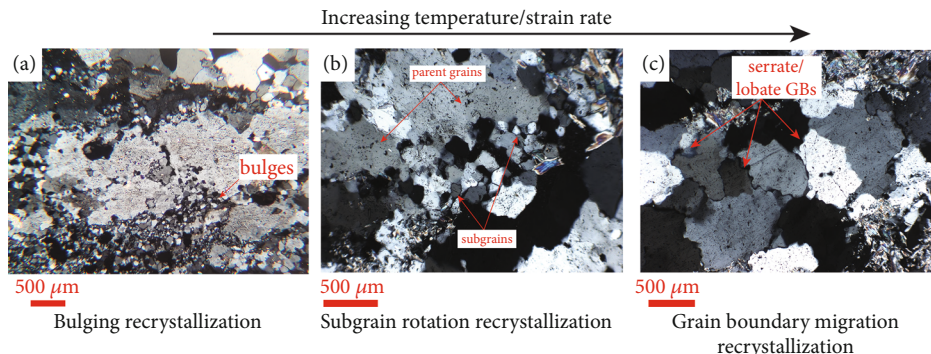


FIGURE 3: Thin section images of representative quartz recrystallization microstructures from a quartz-molybdenite vein (BMA-018-16Fa). The same textures are found in barren quartz veins as well. There are three quartz recrystallization regimes, each of which creates petrographically distinctive grain boundary (GB) microstructures. Pressure, temperature, and stress conditions dictate which regime dominates during quartz deformation. (a) At low temperatures and strain rates, bulging crystallization dominates. Bulging recrystallization results in the formation of strain-free neocrysts along the edges of strained parent crystals. This texture is the least abundant in the Butte samples. (b) At higher temperatures and strain rates, subgrain rotation is the dominant recrystallization mechanism. Subgrain rotation is characterized by polygonal grain boundaries. (c) At even higher temperatures, grain boundary migration is the most active recrystallization mechanism. Grain boundary migration structures are by far the most volumetrically dominant in Butte pre-Main Stage quartz.

Inc.), wherein high resolution visible light scans of thin sections can be calibrated with the sample in the SEM chamber so that the scans can be used for navigation.

**3.2. Correlating CL Intensity with Ti Concentration.** Trace elements can enhance or dampen quartz CL intensity depending on how they distort the crystal lattice. A detailed study of correlations between trace elements and CL intensity of quartz from Butte and other hydrothermal systems was done by Rusk et al. [10], who found that for high temperature quartz ( $>350^{\circ}\text{C}$ ), CL intensity correlates positively with Ti concentration, and that for low temperature quartz ( $<350^{\circ}\text{C}$ ), CL intensity correlates negatively with Al concentration. Titanium solubility in quartz is a function of pressure and temperature [26] but can also be influenced by growth kinetics [27, 28].

CL brightness in an image depends on the gain and offset of the CL detector set by the operator to either emphasize grayscale midtones in the image or to enhance contrast. For any given quartz CL image, it is generally acceptable to interpret the brighter regions as having higher Ti and the darker regions as having lower Ti. However, the correlation between the two is nonlinear, making it difficult to quantify the Ti from CL by interpolation between CL-bright and CL-dark regions [9]. It is likewise misguided to compare CL intensities of different images acquired at different operating conditions. In other words, “bright CL” in one image does not necessarily correspond with the “bright CL” of another.

**3.3. EBSD.** Electron backscatter diffraction data (EBSD) was collected on a composite quartz-molybdenite vein, BMA-023-16Fa. The sample was polished overnight on a vibratory polisher with  $0.05\ \mu\text{m}$  silica grit and a highly napped cloth. Prior to analysis, it was carbon coated with 20 nm of carbon. Automatically indexed electron backscatter diffraction patterns were collected with an Oxford Instruments Symmetry

detector running the Aztec 5.1 software on a Tescan Mira field emission SEM at the University of Lausanne with a 25 kV accelerating voltage and a beam current of 4 nA. The sample was tilted to  $70^{\circ}$  and analyzed at a working distance of 20–25 mm. Patterns were acquired at a step size of  $10\ \mu\text{m}$ . Quartz constituted more than 90 vol.% of indexed phases, accompanied by minor calcite, sericite, and molybdenite. Nonindexed points were grain boundaries, unidentified inclusions, or polishing artefacts such as scratches. Indexing and subsequent cleaning of the data was done using the Aztec software. EBSD data was plotted and analyzed with MTEX [29].

**3.4. Electron Microprobe.** A representative quartz-molybdenite vein (sample BMA-018-16Fa) with no macroscopic evidence of rebreaks, minor amounts of molybdenite, and macroscopically massive quartz was selected for Ti measurements by EPMA. On this sample, 175 Ti analyses on four CL-euhedral and two CL-mottled grains were collected on a Cameca SX100 electron microprobe equipped with five wavelength dispersive spectrometers in CAMCOR at the University of Oregon. The beam was set to a 15 keV energy, 100 nA current, and  $5\ \mu\text{m}$  diameter. Ti K $\alpha$  was measured on all spectrometers, and aggregate mode was turned on. The counting time for Ti K $\alpha$  was 425 seconds for quartz, MgO, NiO, and MnO reference materials. Intensity data were corrected for time dependent intensity loss (or gain) using a self-calibrated correction for Ti K $\alpha$ . Mean atomic number (MAN) background intensity data were calibrated, and the Bremsstrahlung continuum absorption was corrected for Ti K $\alpha$  (see Donovan et al. [30] for details). Unknown and reference material intensities were corrected for deadtime. Reference material intensities were corrected for drift over time. A quantitative blank correction with the quartz reference material as a known unknown was applied. The Main

Stage vein was also analyzed, but all points were below detection limit.

In addition to the quartz-molybdenite and Main Stage veins, two samples of barren quartz stockwork from DH-1A, samples 11052-6121 and 11052-6019 (the last four numbers correspond to the depth of the drill hole the samples are from in feet), were analyzed for Ti, Fe, K, and Al. For these runs, Ti was measured simultaneously on a reference material and on a large pentaerythritol crystal. The beam had 20 keV energy, 200 nA current, and 20  $\mu\text{m}$  diameter. Reference materials were synthetic  $\text{TiO}_2$  for Ti  $\text{K}\alpha$ , orthoclase MAD-10 for Al  $\text{K}\alpha$  and K  $\text{K}\alpha$ , and magnetite U.C. #3380 for Fe  $\text{K}\alpha$ . Counting times were 450 seconds for all elements, and a MAN background was used.

## 4. Results

### 4.1. Hand Sample and Petrographic Characteristics

**4.1.1. Barren Quartz Veins from DH-1A.** The stockwork veins in drill core DH-1A consists of 0.1-7 cm thick, massive, barren quartz. In any given ~10 m of core there are quartz veins with sharply defined planar edges and others with undulose edges (see Appendix (available here)); both coexist with veins that have diffuse gradational contacts that bleed into the country rock. Much of the country rock is intensely silicified or “quartz flooded.” Altered wall rock, whether quartz porphyry or Butte Granite, is altered to gray sericite mineral assemblages and contains, in order of decreasing abundance, quartz, sericite, disseminated pyrite, and trace chalcopyrite. Molybdenite occurs as small (<5 mm) cryptocrystalline blebs near the edges of veins or dispersed throughout the regions of recrystallized quartz.

Barren quartz veins in the stockwork display textures described by Urai et al. [31], and references therein, indicating complete recrystallization, as explained below. Quartz crystals are anhedral, show no crystallographically preferred orientations (CPOs) in the thin section with the quartz plate inserted, and do not exhibit a shape-preferred orientation (Figure 3). Recrystallized quartz grains range in size from 0.05 to 0.2 mm. Grain boundaries are characterized by lobate margins which are broadly indicative of grain boundary migration recrystallization (Figure 3(c)), but features indicative of subgrain rotation (Figure 3(b)) and bulging recrystallization (Figure 3(a)) are also present. There are also small grains that have “foam textures”—quartz with curved grain boundaries and ~120° triple junctions, which are indicative of static recrystallization [2]. Other deformation features include undulose extinction, slightly misoriented domains within crystals, and subgrains decorating grain boundaries. Recrystallized grains contain anhedral fluid inclusions that are randomly distributed throughout (Figure 4(b)). Primary pores are abundant along grain boundaries.

**4.1.2. Quartz-Molybdenite Veins.** Quartz-molybdenite veins are planar and are ~0.1 to 13 cm thick. The veins lack alteration envelopes (see Appendix A2). The walls of smaller, monogenetic quartz-molybdenite veins are lined with 0.1-1 cm CL-euhedral cockscomb quartz, and vein cen-

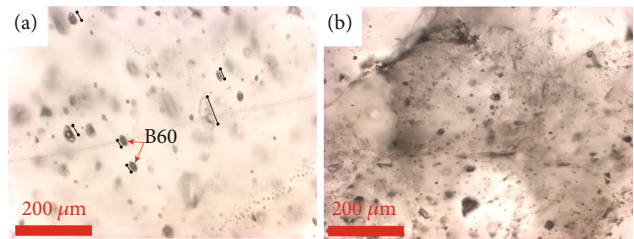


FIGURE 4: There are categorical differences in fluid inclusion morphologies between CL-euhedral and CL-mottled quartz. (a) Fluid inclusions in CL-euhedral quartz are faceted negative crystals oriented parallel to the host crystal *c*-axis. (b) Fluid inclusions in recrystallized, CL-mottled quartz lack faceted morphologies are not parallel to each other and are generally smaller than CL-euhedral quartz fluid inclusions.

ters are filled with equigranular quartz. The *c*-axes of cockscomb quartz crystals are perpendicular to the vein wall, which can be easily seen under the petrographic microscope because the orientation of host crystals is shown by *c*-axis-parallel-aligned euhedral fluid inclusions (Figure 4(a)) [32–34]. The fluid inclusions are types B35 and B60, meaning that, on average, about 35% or 60% of the volume of the fluid inclusion is occupied by a bubble at room temperature (Figure 4; compare Rusk et al. [15]). Composite veins record many rebreaks (similar to syntectonic metamorphic veins) and are much more common than monogenetic quartz veins. Composite veins are basically many monogenetic veins layered together.

Like barren quartz veins, three different grain boundary textures occur in quartz-molybdenite veins (Figure 3). Equigranular quartz grains in vein centers range in size from 20 to 200  $\mu\text{m}$  in diameter, but most are 20 to 70  $\mu\text{m}$  and many have straight grain boundaries. The smaller crystals (20–70  $\mu\text{m}$ ) do not display undulose extinction. Adjacent to these small, nonundulose crystals are larger crystals (100–200  $\mu\text{m}$  along the longest observable axis) that do exhibit undulatory extinction. The grain boundaries of larger grains without neocrysts are serrate or lobate, indicative of grain boundary migration recrystallization. Some recrystallized quartz has a polygonal texture. All recrystallized quartz types contain many small, irregularly shaped fluid inclusions such as those shown in Figure 4(b) as well as unidentified mineral inclusions and planar arrays of secondary fluid inclusions. The anhedral forms of these inclusions are characteristic of fluid inclusions that have been broken and dispersed throughout a crystal during grain boundary migration recrystallization [35]. Where inclusions were intersected during polishing, pock marks are left behind on the polished surfaces.

In larger quartz-molybdenite veins, those exceeding 7 cm thickness, the quartz is distinctly banded with molybdenite (see Appendix A2). Much of the molybdenite is microcrystalline, and it most commonly occurs in thin, discrete layers along the edges of veins and edges of bands within large veins. Some individual molybdenite grains are visible with a hand lens and rarely with the unaided eye. The molybdenite is flecked through fine-grained quartz or is in nearly monomineralic layers. In smaller veins, the molybdenite layers are predominantly planar, but in larger veins, the

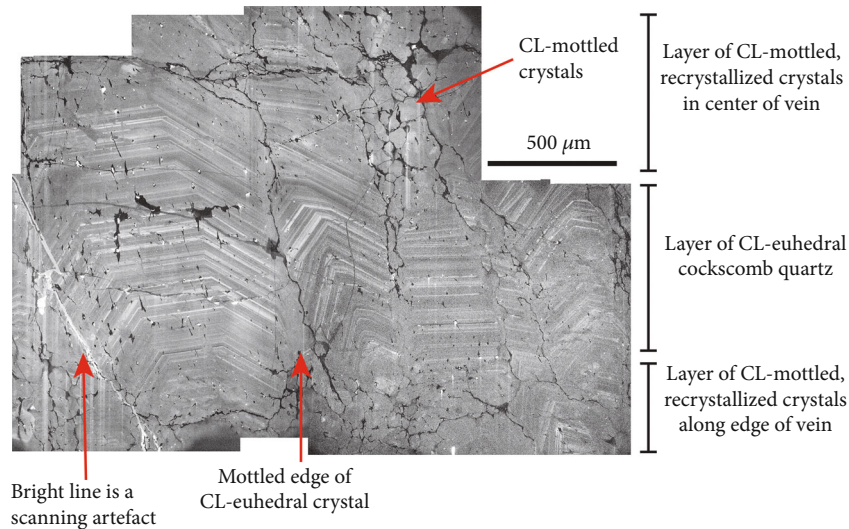


FIGURE 5: The fracture surface that bounds the vein is overlain with a thin layer of CL-mottled recrystallized quartz that underlies a continuous layer of CL-euhedral cockscomb quartz. The cockscomb layer forms by geometric selection, with an initially random layer of crystallites nucleated on the wall rock transitioning into comb quartz as crystals with their *c*-axes projecting into the vein center outgrowing the others. Both layers would have been CL-euhedral when they formed. Centers of veins consist of small-grain quartz that sealed the vein as it precipitated, then subsequently recrystallized to form CL-mottled quartz. The initially randomly oriented layer of crystallites underlying the cockscomb quartz also recrystallized to CL-mottled. During or shortly after vein closure, recrystallization of crystals in easy-glide orientations occurs. Cockscomb quartz crystals are in hard glide orientations and do not undergo wholesale dynamic recrystallization because strain is accommodated by the more easily recrystallized layers at the vein edge and in the vein center. Quartz crystals with CL-euhedral cores and mottled boundaries are common both in the cockscomb layer and as isolated occurrences of CL-euhedral crystals in vein centers. Mottled boundaries of adjacent CL-euhedral cockscomb quartz grains may form by localized, thermally activated recrystallization of grain boundaries driven by surface free energy minimization where there are small amounts of lattice mismatch between adjacent, subparallel crystals. The original growth boundary is imperfect but begins to approach a stable geometrical configuration when annealed. The bright linear feature in the lower left corner of the CL image is a fracture, and the vertical streaks below it are a scanning artefact of the SEM, as are the similar vertical bright streaks cutting the mottled grains at the lower right of the image.

molybdenite layers are arcuate and smeared through the interior of the quartz vein, creating a marbled appearance (see A2 in Appendix). Microscopic flecks of molybdenite are also dispersed throughout quartz-rich regions. Layer thicknesses range from ~0.2 to 2 cm in the large, banded veins.

**4.1.3. Shallow Main Stage Vein.** The Main Stage vein (sample BMA-020-16Fa) from the easternmost Continental Pit (blue star in Figure 1(a)) is 2 cm wide and contains quartz that lacks undulatory extinction and recrystallization microstructures. The wall rock is pervasively altered to a white argillite assemblage that includes residual abundant chalcopyrite and primary biotite. The vein is symmetrically zoned from an outermost 2 mm layer of microcrystalline milky quartz, overlain by a <1 mm layer of clearer microcrystalline quartz, and a third <1 mm layer of milky quartz from which macroscopically euhedral 0.3 to 2 mm comb quartz crystals project into vugs in the center of the vein, some of which contain chalcopyrite, pyrite, and bornite—a common Main Stage assemblage.

#### 4.2. SEM-CL

**4.2.1. Barren Quartz/Quartz-Molybdenite CL Textures.** Barren quartz vein samples from DH-1A are entirely CL-

mottled. The quartz-molybdenite vein from the eastern Pittsmont dome (sample BMA-018-16Fa; red star in the Continental Pit area of Figure 1(a)) has the following symmetrically developed sequence of textures from the edges to the centers: wall rock fracture surface, a 0.01 mm layer of CL-mottled crystals, a 0.5–2 mm layer of cockscomb CL-euhedral quartz crystals, and a central layer of CL-mottled grains (Figure 5). Oscillatory zones are continuous from one crystal to the next along cockscomb layers (Figure 5). Most growth zones in CL-euhedral crystals are 10 to 15  $\mu\text{m}$  thick, but they range in thickness from 25  $\mu\text{m}$  to <1  $\mu\text{m}$ , and most CL-bright bands have sharp boundaries against adjacent CL-dark bands (Figures 2(a) and 5).

Some CL-euhedral crystals have mottled edges (Figure 5). CL-mottled crystals ranging in size from 10 to 30  $\mu\text{m}$  fill the centers of veins and dominate the volumetric bulk. Some crystals in the center zone have a “ghost band” CL texture that is visually intermediate between CL-euhedral and CL-mottled (Figure 2(b)), wherein what appear to be relict bright bands of CL-euhedral texture have been modified by diffusion. Isolated CL-euhedral crystals with mottled edges can be found in vein centers surrounded by CL-mottled crystals.

**4.2.2. Shallow Main Stage Vein CL Textures.** The Main Stage quartz vein displays breccia and cockscomb quartz textures

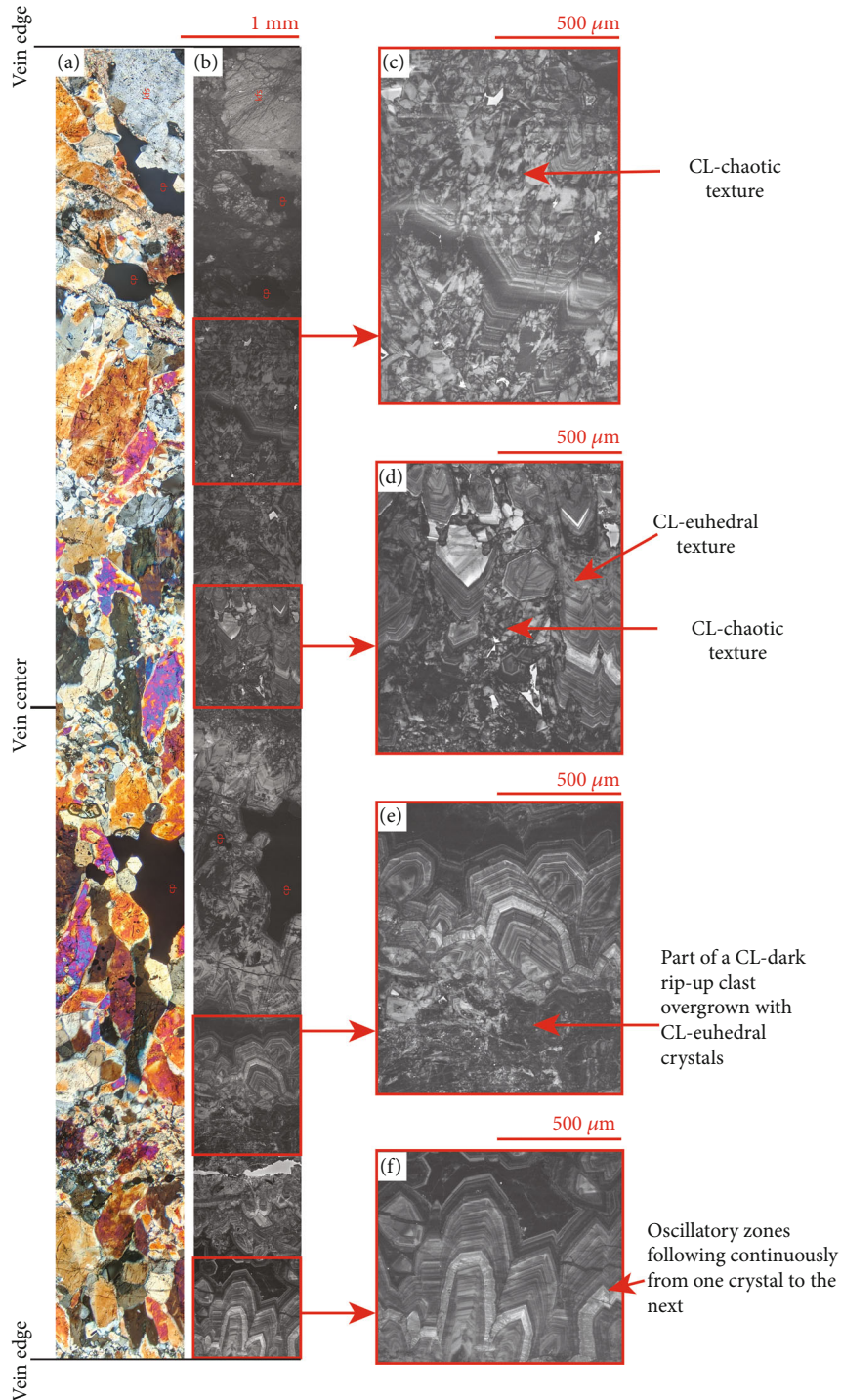


FIGURE 6: CL textures in low temperature Main Stage quartz are much more complex than those in higher temperature pre-Main Stage quartz. (a) A thick section transect of Main Stage quartz; all crystals are quartz unless labelled otherwise. cp: chalcopyrite; kfs: K-feldspar. (b) The same transect imaged in CL. (c–f) Close-ups of regions from (b).

(Figure 6). Layers of cockscomb quartz exhibit euhedral oscillations that are unambiguously continuous from one crystal to the next (labelled as “oscillatory zones that follow continuously from one crystal to the next” in Figure 6(f) and seen also in the upper portion of Figure 6(e)). In the center of the vein are smaller euhedral quartz crystals with banding patterns in their cores. These cores of single crystals

are encrusted in rims whose banding patterns track from one crystal to the next (Figure 6 panels). In addition, the vein center contains clasts that appear to be rip-ups of an early generation of dark CL-homogeneous quartz (Figure 6(e)). The interpretation of these clasts as rip-ups is supported by the presence of larger clasts of preexisting veins that are incorporated into Main Stage veins at hand sample and

outcrop scales. These CL-homogeneous clasts are overgrown with CL-euhedral crustiform quartz that appears to match the encrusting quartz otherwise in the center of the vein (Appendix section A4).

Other textures include sharply defined, angular domains of mixed and patchy CL-bright and dark quartz (Figures 6(c)–6(e)), hereafter referred to as CL-chaotic (see also Appendix section A4). Heterogeneity in the CL-bright domains occurs as CL-gray feathers or wavy regions with slightly less CL intensity. In some regions, CL-bright domains are plumose or flame-like. Regions of CL-euhedral quartz occur sporadically within chaotic regions. It is notable that, despite the complexity and small scale of the CL-chaotic texture, it is not formed of clusters of micro-crystals. In other words, in the thin section (Figure 6(a)), CL-chaotic crystals are optically continuous and relatively large (100–500 µm) while CL-bright and dark domains in that same optically continuous crystal are much smaller (20–80 µm).

**4.2.3. Late Stage Microfracturing.** In all quartz veins imaged, there are ubiquitous late-stage microfractures that cut CL-mottled and CL-euhedral grains alike (Figures 2, 5, 6, and 7; see also Rusk et al. [10]). Similarly, CL-dark rinds are common along the grain boundaries of CL-mottled crystals (Figure 7). Because these fractures cut both CL-mottled and CL-euhedral crystals, they are later than both of them and not further considered here.

**4.3. EBSD.** An EBSD map (Figure 8(a)) of a composite quartz-molybdenite vein from the Continental Pit (BMA-023-16Fa; red star in Figure 1) shows the distribution of randomly oriented CL-mottled crystals along with a preserved layer of CL-euhedral crystals. Figure 8(b) shows a thin section in cross-polarized light with a layer of cocks-comb quartz outlined in red. That same layer is outlined by an inset in quartz orientation maps (Figures 8(a) and 8(c)), a map showing the grain orientation spread (Figure 8(d)), and is shown in CL in Figure 8(e). The correlated misorientation diagram indicates the presence of Dauphiné twins, as shown by a large peak at 60° (Figure 8(f)). The uncorrelated misorientation diagram shows that the overall texture of the mapped region is close to random (Figure 8(g)).

Overall, the EBSD data shows that there are small layers of quartz where the crystals are oriented subparallel to one another but that the majority of vein quartz is randomly oriented.

**4.4. Electron Microprobe.** We analyzed CL-mottled crystals and bright and dark growth bands of CL-euhedral textures and found the largest range in Ti concentrations in CL-euhedral crystals of the quartz-molybdenite vein from the Continental Pit (BMA-018-16Fa). Ti concentrations in four crystals ( $n = 132$ ) range from 17 to 323 ppm in the bright domains with a mean of  $80 \pm 63$  ppm Ti and 16 to 40 ppm Ti in the dark domains with a mean of  $25 \pm 8$  ppm Ti. Two crystals have CL-euhedral cores that grade into CL-mottled edges with slightly elevated Ti concentrations compared

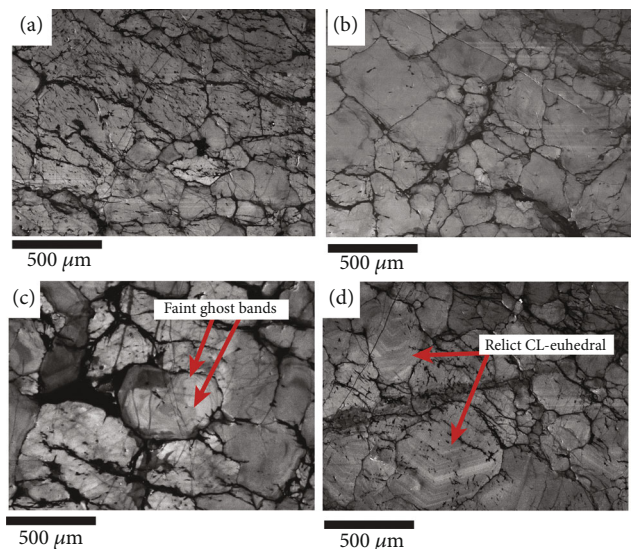


FIGURE 7: CL images of composite quartz-molybdenite vein (BMA-023-16Fa) from the Continental Pit. (a) CL-mottled region with extensive late fractures. (b) CL-mottled crystals with fewer intercrystalline fractures, but CL-dark quartz along grain boundaries indicates late infiltrative fluid flux. (c) CL-bright ghost band in a crystal with microfractures cutting through it. (d) two relict CL-euhedral crystals in a region that is otherwise dominated by CL-mottled quartz; both CL-euhedral and CL-mottled quartz are cut by late stage fractures.

to contiguous, entirely CL-mottled crystals. These CL-mottled crystals contain 23 to 47 ppm Ti with a mean of  $31 \pm 6$  ppm Ti. Mottled edges of crystals with CL-euhedral cores have between 7 and 45 ppm Ti with mean of  $29 \pm 9$  ppm Ti. Quartz in barren quartz veins, all of which is CL-mottled, ranges from 99 ppm Ti to below the detection limit and has a mean concentration of  $37 \pm 19$  ppm Ti ( $n = 79$ ). Analytical uncertainty on individual data points is a maximum of  $\pm 4$  ppm Ti, and variation due to measurement error is small compared to the spread of Ti concentrations. Ti concentrations, errors, and sampling statistics are shown in Figure 9 and are available for download in the Electronic Materials. All Ti measurements from the Main Stage sample BMA-020-16Fa are below the detection limit of 7 ppm ( $n = 43$ ), which confirms the below-detection microprobe Ti results for Main Stage quartz that Rusk et al. [10] reported.

## 5. Discussion

**5.1. Quartz Precipitation Temperatures.** Ti concentrations in quartz can be used to estimate temperatures of quartz crystallization. In a previous paper, we showed that the Huang and Audétat [27] calibration yields temperatures that are consistent with independent estimates for samples from Butte and several other well-constrained igneous systems (see Figure 1 of Acosta et al. [28]). We assume the fluid is at rutile saturation (i.e., the activity of  $TiO_2$  is fixed at unity) because rutile is abundant in barren quartz and quartz-molybdenite veins. All temperature estimates reported

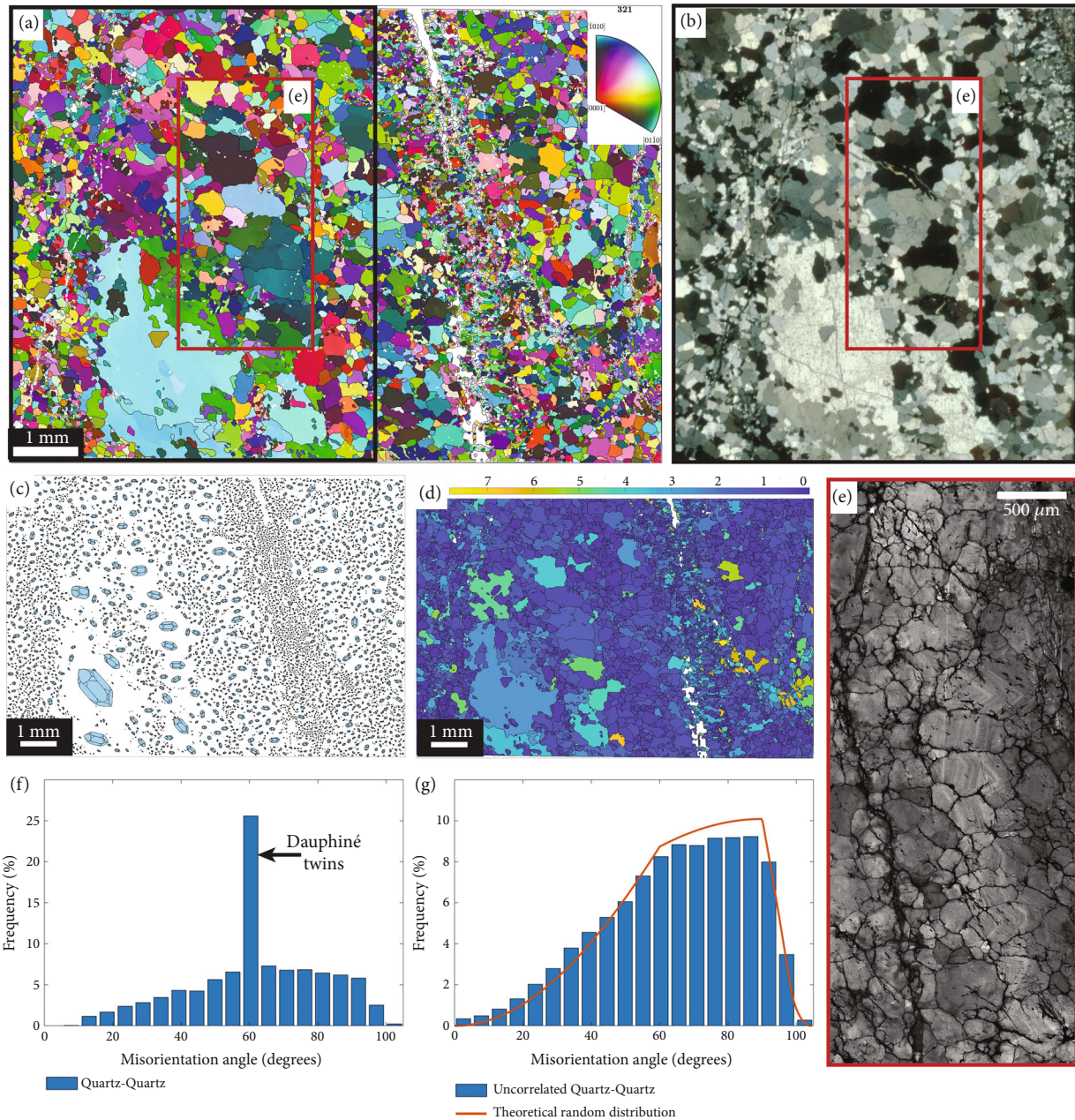


FIGURE 8: EBSD and petrographic images of composite quartz-molybdenite vein BMA-023-16Fa. The red rectangular area inset outlined in (a) and (b) is the region shown in CL in (e). The area outlined in black in the EBSD orientation map (a) corresponds to the region shown in cross-polarized light in (b). In thin section, it can be seen that the subparallel cockscomb quartz crystals do not exhibit undulose extinction. The majority of crystals in the sample have a random orientation, as seen in (a) and (c) and are CL-mottled. (d) shows the grain orientation spread of the sample, which is the average of the misorientation angles to the average grain orientation. Note that in both (a) and (d), the oriented cockscomb quartz does appear to have domains of slightly different orientation, but that these are insufficient to cause undulose extinction as seen in (b). The layer of cockscomb quartz is CL-euhedral (e); interestingly, the apparent grain boundaries imaged in CL do not appear to correspond to those observed in the thin section or in the EBSD grain reconstructions, as was also observed in Figure 6. (f) and (g) are correlated and uncorrelated misorientation angle distributions, respectively. Because the sample is dominated by recrystallized CL-mottled quartz, the few oriented cockscomb quartz crystals are insufficient to skew the overall distribution away from random.

herein are calculated using a lithostatic pressure of 2.5 kbar based on the fluid inclusion analyses of Rusk et al. [15] and Roberts [13]. Calculations at a hydrostatic pressure of 0.63 kbar yield temperature estimates that are  $\sim 83^{\circ}\text{C}$  lower.

Previous temperature estimates of barren quartz/quartz-molybdenite veins range from 500 to  $700^{\circ}\text{C}$  using three different thermometers. Roberts [13] used coexisting ilmenite-hematite pairs to constrain the temperature to 550– $700^{\circ}\text{C}$ . Brimhall [23] used K-Na partitioning in K-feldspar

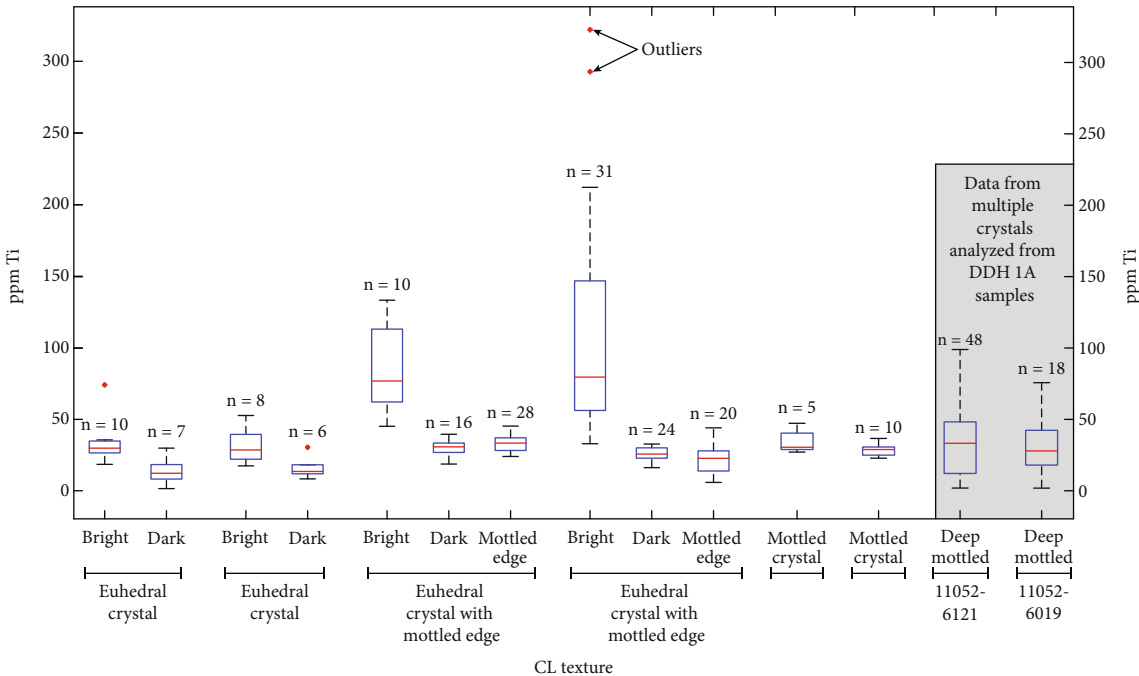


FIGURE 9: On a single quartz-molybdenite vein (BMA-018-16Fa), Ti EPMA measurements were made on bright and dark growth bands of CL-euhedral crystals, euhedral crystals with mottled edges, and mottled crystals. Individual crystals are demarcated by horizontal lines below the  $x$ -axis. Data within the gray box is on entirely CL-mottled quartz from two barren quartz veins (sample numbers labeled on graph) in the drill core. Note that “bright” and “dark” are relative terms and depend on user-specified operating conditions at the time of CL image acquisition. The maximum error on individual analysis points is  $\pm 4$  ppm Ti, which is insignificant compared to the range of values.

and muscovite to constrain the temperature to 550–700°C as well. Field et al. [36] used S isotopes of coexisting sulfide mineral pairs to estimate quartz-molybdenite temperatures of 500–630°C.

Combining the Ti-in-quartz Mercer and Reed [37] dataset with ours gives an average of 48 ppm Ti and a temperature of 660°C for barren quartz veins. We note that the Mercer and Reed [37] dataset is made up of seven barren quartz samples taken from four different drill holes, and so, the variability in their data is probably due in part to natural variations in the temperatures of formation of individual veins.

The quartz-molybdenite vein from the Continental Pit gives temperatures ranging from 499 to 907°C (Figure 9). The highest temperatures are from CL-euhedral bright bands and are unrealistic given the fluid temperature estimates outlined above, indicating that these bands have Ti in excess of the equilibrium concentration. In contrast, an average Ti of 25 ppm in CL-euhedral dark bands corresponds to 600°C. Averages of 29 ppm Ti for mottled edges and 31 ppm Ti for mottled crystals yield respective temperatures of 612°C and 619°C. An average of 37 ppm Ti from mottled quartz in barren quartz veins from DH-1A corresponds to a temperature of 635°C. It is unlikely that the deformation that resulted in CL-mottled textures occurred at a temperature significantly higher than that of quartz precipitation. Barren quartz/quartz molybdenite veins are thus estimated to have formed and deformed at temperatures between 600°C and 635°C.

The maximum Ti concentration of 99 ppm in barren quartz corresponds to a near-magmatic temperature of 741°C at 2.5 kbar, which is a reasonable upper limit given that some deep barren quartz veins adjacent to the cupola have aplitic centers and contain a mixture of fluid and melt inclusions (not examined in this study) [13, 15]. Overall, temperature estimates for CL-mottled and the dark bands of CL-euhedral quartz made using the Huang and Audébat [27] calibration of the TitaniQ thermobarometer are in good agreement with independent temperature constraints.

**5.2. Quartz Recrystallization.** The strain that transforms CL-euhedral to CL-mottled can be interpreted using the substantial body of work on quartz recrystallization and how different processes are expressed in measurable quantities such as crystal shapes, crystal size distributions, and crystallographic preferred orientations (CPOs).

Bulging recrystallization occurs between 250°C and 400°C and is a common outcome of high strain rates [4]. As a bulge ripens, it becomes a discrete small grain, so this regime produces a bimodal grain size distribution wherein larger crystals are mantled by new small crystals (core-and-mantle structures; Figure 3(a)). Subgrain rotation occurs between 400°C and 500°C [31] and is characterized by straight grain boundaries and, in some instances, a bimodal crystal size distribution. Grain boundary migration is active above about 500–600°C and can result in coarse crystals with lobate and serrate grain boundaries [4, 38]. Grain boundary migration in an isotropic stress field is also the mechanism

for quartz annealing/polygonization, whereby equilibrium foam structures characterized by curved grain boundaries and 120° triple junctions form [39]. Regardless of whether grain boundary migration created lobate grain boundaries or foamy grain boundaries, we find that all CL-mottled grains have grain boundary recrystallization microstructures.

Recrystallization changes initial crystal size distributions as a function of recrystallization mechanism and differential stress. During recrystallization, some grains grow at the expense of others, which can produce an equilibrium grain size distribution that may be finer- or coarser-grained than the initial one. Recrystallization can result in grain size reduction and subsequent mechanical weakening [40, 41] but can also result in grain coarsening and strength hardening [41]. However, interpreting recrystallization crystal size distributions in natural samples is difficult because of overprinting during cooling, a potential dependence on water activity, misinterpretation of the dominant recrystallization mechanism, the presence of secondary minerals that can pin otherwise mobile grain boundaries, and heterogeneous strain accommodation [2].

Grain boundary sliding, the movement of grains relative to one another, may accompany quartz recrystallization [42, 43] at low strain rates and high temperatures. Grain boundary sliding can also operate at low stresses in dilatant systems where it can be accommodated by cataclasis and particulate flow [42]. The sliding may prevent the formation of a crystallographically preferred orientation (CPO) or destroy an existing CPO [44, 45] and may randomize grain boundary misorientation axes [46]. The presence of pores along grain boundaries and small grain sizes can facilitate grain boundary sliding [2, 47].

The initial crystal size distribution also exerts a control on material strength during ductile deformation. Typically, materials that are coarser grained are stronger than materials that are finer grained which are less cohesive. The opposite can also be true when deformation occurs mostly as dislocations moving through a crystal; grain boundaries stop dislocations, so dislocation movement is limited by the density of grain boundaries (Hall-Petch strengthening).

**5.3. Easy vs. Hard Slip Orientations.** A brief review of quartz slip features here provides a basis for interpretations explained below. At low strain rates and temperatures below ~650°C, basal slip (perpendicular to the *c*-axis) is the dominant slip system in quartz [48–50]. At higher temperatures and strain rates, *c*-slip (slip parallel to the *c*-axis) is the dominant slip system. A given crystal may deform plastically by either of these slip systems in a deviatoric stress field depending on its orientation. The resolved shear stress, the effective shear acting on a slip plane, is maximized when  $\sigma_1$  is 45° from the slip plane and minimized when  $\sigma_1$  is perpendicular to the slip plane [51]. For the relevant temperature range (~650°C), quartz could slip along either the basal or prism planes. A crystal is said to be in an easy glide orientation if it is oriented in a given stress field such that the resolved shear stress on a given slip plane is higher than the critical resolved shear stress, which is the effective shear needed to activate glide on a given slip plane. A crystal is

said to be in a hard glide orientation if it is oriented in a given stress field such that the resolved shear stress on a given slip plane is less than the critical resolved shear stress.

**5.4. Crystallographic Twinning.** The only twins found in the EBSD data are Dauphiné twins (Figure 8(f)). Dauphiné twinning is defined by a 180° axis rotation about the *c*-axis [0001] of quartz, and it has no effect on the orientation of the crystallographic axes of the crystals, meaning that adjacent Dauphiné-twinned crystals are in the same hard- or easy-glide positions relative to one another and deform identically because the orientations of glide systems are the same in both [52, 53]. The existence of Dauphiné twins in cocks-comb quartz layers does not alter the response to an applied shear stress but can be used to place additional constraints on the temperature of quartz growth.

Dauphiné twins can be primary growth twins, mechanical twins, or transformational twins. Mechanical twins form during deformation. Transformational twins form during cooling through the  $\alpha$ - $\beta$  transition temperature. In  $\beta$  quartz, *m*-faces are absent or extremely poorly developed, and the *r*- and *z*-faces become crystallographically and morphologically equivalent [54]. Cockscomb quartz Dauphiné twins did not form by cooling because we can see the trace of prism faces and distinguish between *r*- and *z*-faces in Butte vein quartz. Because the  $\alpha$ - $\beta$  transition is displacive, meaning that it is just a slight change in bond angle and requires no breaking or making of covalent bonds, CL textures are unaffected by the phase change. Thus, the cocks-comb quartz formed below the  $\alpha$ - $\beta$  transition temperature, which corresponds to 638°C at 2.5 kbar or 590°C at 0.62 kbar [55]. Since quartz recrystallizes at the same (or similar) temperature as growth (see below), the Dauphiné twins in recrystallized quartz are likely a combination of growth and mechanical twins.

### 5.5. Interpretations

**5.5.1. CL-Dark Euhedral Bands Preserve Equilibrium Ti Concentration.** The CL-dark bands record near equilibrium growth, and the high-Ti bright bands reflect excursions away from equilibrium, as supported by the following observations: (1) CL-dark euhedral bands have roughly the same amount of Ti from one dark band to the next, whereas Ti concentrations in bright growth bands are higher and wider-ranging (Figure 9). (2) The TitaniQ temperature estimates for dark bands and CL-mottled crystals are in good agreement with each other and with independent temperature estimates using other geothermobarometers. (3) Ti concentrations in dark bands are similar to those in nearby recrystallized CL-mottled crystals. This last observation is discussed in more detail in the section below.

The unrealistically high temperature estimates of CL-bright quartz bands suggests that they contain Ti in excess of the equilibrium value. Fast growth is expected to increase the uptake of Ti [27, 28], and one possibility is that CL-bright bands form during pressure fluctuations that are relatively short-lived but cause fast quartz growth.

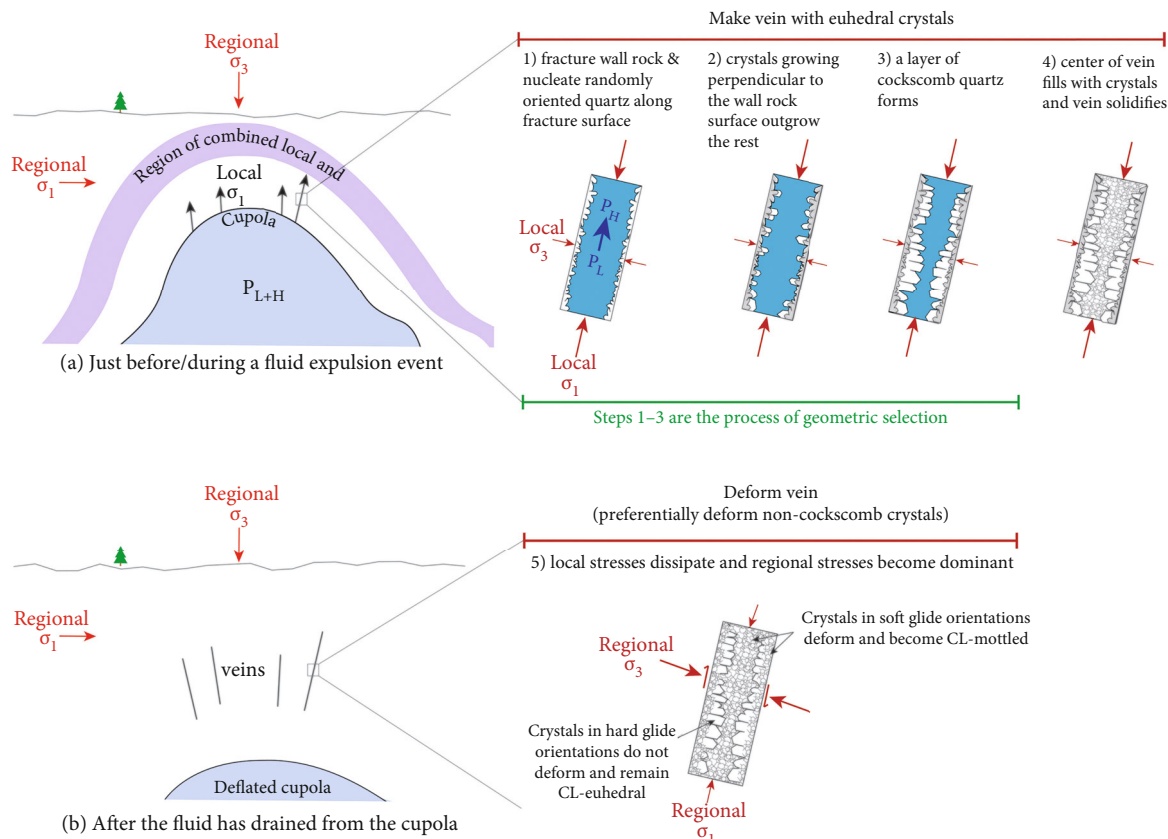


FIGURE 10: The suggested sequence of crystal growth and deformation for the formation of a monogenetic quartz vein as discussed in the interpretative section of the main text consists of hydrofracture-driven crack growth and fluid influx followed by quartz precipitation from a fluid, sealing of the vein with quartz, and changes in the local stress regime. Initially, when a hydrofracture forms, it is in response to a nonvertical local stress regime imposed by the cupola/magma chamber. The initial strikes of hydrofractures are perpendicular to the outermost edge of the cupola. As local stresses dissipate, nonvertical veins shear as regional stresses take over. Any nonnormal stress results in shear strain as the stress rotates.

**5.5.2. Origin of CL-Mottled Texture and Coexistence of CL-Mottled and CL-Euhedral Textures.** It is accepted that CL-euhedral quartz grains are primary crystals precipitated from a hydrothermal solution, but the origin of coexisting CL-mottled crystals is less obvious. CL-mottled crystals display undulose extinction in the thin section and have grain boundary forms indicative of recrystallization, indicating that CL-mottled quartz may form by deformation of CL-euhedral quartz with consequent smearing (ghost band textures are discussed in a separate section below) or obliteration of growth zonations. This raises the question: why do some CL-euhedral crystals escape deformation?

Cockscomb quartz forms by the process of geometric selection, also known as competitive grain growth, which has been studied extensively by geologists and chemists [56–60]. In the process of geometric selection, an initial nucleation along a substrate creates a layer of randomly oriented crystals nucleated on the fracture surface (Figure 10(a), step 1) [60, 61]. Crystals that happen to be oriented with  $c$ -axes perpendicular to the fracture surface outgrow the others because their tips protrude into the cavity where the supply of silica from the fluid is most readily

available (Figure 10(a), step 2), resulting in a layer of large, subparallel crystals (Figure 10(a), step 3) [62, 63]. This creates cockscomb quartz, which can form from fluids at low degrees of quartz supersaturation that undergo either slow or mild fluctuations in growth conditions such as pressure or temperature [59, 64, 65].

In contrast to the edges of quartz-molybdenite veins being cockscomb quartz, the vein centers are made of anhedral, equigranular, CL-mottled quartz. The equigranular quartz in vein centers may precipitate *in situ* but not as epitaxial overgrowths on cockscomb quartz, or the quartz grains may nucleate higher or lower in the vein fluid, then accumulate in the vein center. None of these would result in a crystallographically preferred orientation in the centers of veins; i.e., vein centers would have initially had crystals in both hard and easy glide orientations (Figure 10(a), step 4).

We infer that after the veins were filled but before they cooled, recrystallization at high temperature deformed CL-euhedral quartz in vein centers to CL-mottled quartz. Our data showing that Ti concentrations in CL-mottled crystals is roughly the same as those in the dark bands of adjacent

CL-euhedral crystals indicates that deformation temperatures were nearly the same as the temperature of primary crystallization of CL-dark bands. Recrystallization was dominated by grain boundary migration at low differential stress. Grain boundary migration reset quartz towards the equilibrium Ti concentration for the recrystallization temperature. Volume diffusion of Ti through quartz is very slow [66, 67], but strain-induced grain boundary migration can reset Ti in quartz towards a new equilibrium value at a rate that is much faster [68–70] especially in fluid-rich systems such as Butte [71]. Lower temperature recrystallization mechanisms—subgrain rotation and bulging recrystallization—can reset Ti to lower equilibrium values in certain conditions [71] but are generally much less likely to do so [71, 72]. Haertel et al. [73] found that synkinematic quartz veins that underwent retrograde bulging and subgrain rotation recrystallization during exhumation at temperatures less than 350°C preserved Ti concentrations and gave thermometric estimates that were a close approximation of the temperature of original vein formation. Thus, we infer that the CL-mottled texture and attendant Ti resetting occurred during high temperature grain boundary migration recrystallization and that subsequent lower temperature bulging and subgrain rotation recrystallization must have occurred during vein cooling and exhumation but did not further facilitate Ti loss and equilibration.

For cockscomb quartz layers, basal glide would occur parallel to the vein edge (and perpendicular to the *c*-axis) and prism glide would be perpendicular to the vein edge (and parallel to the *c*-axis). Cockscomb quartz is thus a layer of hard glide-oriented crystals with respect to the expected paleostresses (Figure 10(b), step 5) and also with respect to both possibly active slip systems. Crystals sandwiching the cockscomb quartz were initially in a variety of hard and easy glide orientations. As stresses acting on the vein fluctuate from local, magma chamber-related stresses to regional stresses, easy glide-oriented crystals will preferentially accommodate deformation. Glide fails to occur in cockscomb crystals because the shear stress on the potentially active glide planes of cockscomb quartz is less than the critical stress needed for slip to occur. In contrast, quartz crystals in layers above and below the layer of cockscomb quartz are initially in a combination of hard and easy glide orientations, because no primary growth process could have produced a strong CPO in these layers. At the onset of deformation, easy glide-oriented quartz grains deform first. As they deform around crystals in hard glide orientations, the hard glide-oriented crystals rotate into easy glide orientations until they too deform plastically [74]. Thus, strain is preferentially accommodated in the noncockscomb quartz layers that sandwich cockscomb quartz, leaving the cockscomb quartz relatively intact (Figure 10(b), step 5). Stated another way, the cockscomb quartz layer is rheologically stronger than the noncockscomb quartz layers. A similar conclusion was reached by Toy et al. [75] in their investigation of the Alpine Fault Zone mylonites from New Zealand. Toy et al. [75] found that quartz crystallographic orientations developed in early deformation events controlled which slip systems were activated during subse-

quent deformation and, thus, whether or not the early fabric was preserved or overprinted. Preferential deformation due to crystal orientation has been shown to occur in peridotite [76], metallurgical samples [77], and deforming ice. For example, polycrystalline aggregates of ice, which is also in the hexagonal crystal system and is generally accepted to deform analogously to quartz, undergo preferential deformation of easy glide-orientated crystals in glaciers [78, 79]. Marmo and Wilson [80] showed that a vein made of oriented columnar ice crystals in hard glide orientations remained undeformed during glacial flow as strain was accommodated in the surrounding easy glide-oriented ice. Bestmann et al. [71] also showed that the crystallographic orientation of quartz in metamorphic veins determined whether a crystal persisted as a relatively unstrained porphyroblast or was deformed into ribbon or mylonitic quartz. These results highlight the role that growth fabrics can have on rock strength during ductile deformation.

Another possible reason for the difference in relative strengths between cockscomb quartz and vein interiors could be starting grain size. However, because recrystallization modified the crystal size distribution of vein interiors via grain boundary migration, we cannot speculate as to what the initial crystal size distribution was and how it influenced subsequent heterogeneous strain accommodation. CL-euhedral cockscomb crystals are much larger than CL-mottled crystals, but this could be due to grain size reduction of CL-mottled crystals during recrystallization and cannot be used as evidence that CL-mottled crystals were initially larger or smaller than CL-euhedral ones.

Barren quartz veins, which occur deeper in the system and grade upward into quartz-molybdenite veins, are completely lacking in CL-euhedral crystals. It is possible that cockscomb quartz did not form at depth. It is also possible that these veins lack cockscomb quartz because they underwent more recrystallization than their shallow counterparts owing to their proximity to the cupola. More intense deformation of barren quartz veins would also explain the observation that many of them have undulating vein forms—initially planar veins could have undergone weak folding during cupola inflation and deflation cycles.

When cupola fluids are overpressurized, there is a localized zone around the cupola where the stress field is dominated by cupola-imposed stresses. The wall rock adjacent to the cupola is also hot and relatively ductile owing to its proximity to the magma chamber. Far from the overpressurized cupola, stress is regional, which was compressive with a horizontal  $\sigma_1$  in Butte [16]. Between the cupola stress field and the far-field tectonic forces is a zone where the stress is a summation of the two. In the proximity of this zone, stress orientation would fluctuate (Figure 10(b), step 5) as the cupola inflates, hydrofractures, deflates, and reinflates [81]. Thus, veins emplaced in the zone of combined regional and local stresses undergo localized deformation as cupola stresses change. This may be accompanied by collapse of the deflated cupola or subsequent rotation of the vein as a block during later fluid expulsions.

To summarize, early quartz veins in Butte formed by the following:

- (1) Hydrofracturing rock around the magma chamber cupola to create dilatant fractures filled with fluid
- (2) Growth of cockscomb quartz by geometric selection (Figure 10(a), steps 1-3) wherein crystals with  $c$ -axes perpendicular to the wall rock substrate outgrow the others, creating a layer of parallel crystals
- (3) Solidification of the center of the vein (Figure 10(a), step 4) where euhedral, homogeneously nucleated, and randomly oriented crystals jam or settle in the centers of veins, thereby plugging the vein
- (4) Grain boundary migration and dissolution-precipitation recrystallization of veins in the cupola and its halo (Figure 10(b), step 5)
  - (a) Barren quartz veins are abundant in and next to the cupola where high temperatures enable ductile strain, causing veins to recrystallize to CL-mottled textures
  - (b) Quartz-molybdenite veins are exterior to the cupola where the stress regime is produced by a combination of regional and cupola pressurization effects. In contrast to the cupola, this zone is less ductile and transient shear stresses arise from cupola inflation and deflation. After a vein is mostly solidified, noncockscomb layers of quartz in the vein accommodate stress by rotating and deforming plastically, converting CL-euhedral textures to CL-mottled textures. Strain preferentially afflicts crystals in the centers of veins, sparing relatively strong layers of cockscomb quartz at the vein edges. The randomly oriented crystals lining the vein margin also recrystallize, leaving only the cockscomb layers intact
- (5) Local low-temperature recrystallization occurs as the pluton and its hydrothermal system cooled. Subgrain rotation and bulging recrystallization do not affect Ti concentrations in quartz

**5.5.3. Lack of Crystallographically Preferred Orientation (CPO) in CL-Mottled Crystals.** The lack of a CPO in recrystallized, CL-mottled vein interiors could be explained in two ways. One is that the initially random crystal configuration in vein interiors stayed random, i.e., that the majority of recrystallization occurred in an isotropic stress field or in a stress field where the magnitude of deviatoric stresses were small. This is our preferred hypothesis because the textures do not indicate large differential stresses. An alternative hypothesis is that grain boundary sliding in a dilatant, fluid-flushed system destroyed or prevented the formation of an extensive CPO.

**5.5.4. Mottled Edges of Cockscomb CL-Euhedral Crystals.** We speculate that mottled edges of cockscomb CL-euhedral crystals (Figure 4) form because the lattices of adjacent crystals do not align during competitive grain growth, yielding irregular boundaries with a large surface free energy [58]. Impingement of one crystal into the next can also generate intracrystalline strain (the so-called force of crystallization). This phenomenon of growth boundary mismatch is caused by variation in relative growth rates of individual faces as the crystals impinged on one another [58]. Those boundaries then recrystallize during localized grain boundary migration, driven by surface free energy minimization or minimization of intragranular strain, or via dissolution-precipitation recrystallization. If recrystallization operates by grain boundary migration, then motion would be driven by strain within the grain being consumed which would explain the lobate grain boundary and apparently unidirectional motion of grain boundaries.

**5.5.5. Formation of Ghost Bands.** We consider three possible mechanisms for the formation of the ghost band texture (Figures 2(b) and 7(c)): (1) each blurred layer formed via precipitation from quartz-saturated grain boundary fluids during recrystallization, (2) pipe diffusion of initially CL-euhedral crystals blurred the once sharp boundaries between growth layers, and (3) grain boundary migration of initially CL-euhedral crystals blurred the once sharp boundaries between growth layers.

Because it is reasonable to assume that the hydrothermal vein-sealing quartz is initially CL-euhedral, we prefer the interpretation that ghost band textures form by way of Ti diffusion through quartz and subsequent blurring of euhedral growth bands. Although volume diffusion of Ti through quartz is too slow to blur the CL-euhedral bands [67], Ti diffusion through quartz can be mediated by grain boundary migration or through pipe diffusion. In the former case, Ti is redistributed through the quartz structure as grain boundaries sweep through. Fluid inclusion sizes and shapes are modified concurrently, resulting in the irregular appearance of fluid inclusions seen in recrystallized, CL-mottled quartz (Figure 3(b)) [35]. In the latter case, Ti preferentially diffuses along interconnected dislocations. This process is called “pipe diffusion” [82] and has been documented as blurring CL growth bands in zircon [83]. Because the ghost band texture is found in crystals that have equilibrium “foam” grain boundary geometries, we favor the interpretation that the texture forms as grain boundary migration facilitated Ti diffusion in an initially CL-euhedral crystal. Thus, the ghost band texture is intermediate between the two end-member textures of unrecrystallized CL-euhedral and completely recrystallized CL-mottled. We speculate that if deformation had continued, the ghost band texture would become CL-mottled texture as Ti continued to diffuse and homogenize in the grain.

Holness and Watt [84] and Piazolo et al. [39] reported ghost band textures in contact metamorphic quartz from the Ballachulish contact aureole. Both studies concluded that the texture of subparallel bands formed during grain boundary migration, wherein each bright band represents a single

growth stage. In this framework, the grain boundary migrated in a direction perpendicular to the ghost bands. Holness and Watt [84] report that the country rock is CL-mottled but also note that it underwent regional metamorphism. It is possible that the ghost bands they document formed as quartz dissolved or melted (both studies report evidence of partial melting) due to heating in the contact aureole and then reprecipitated as oscillatory overgrowths on relict CL-mottled grains as the contact aureole cooled. Ghost band texture was also reported in a shallow porphyry deposit by Müller et al. [25], but the relict cores are CL-euhedral. In this case, it is apparent that the diffuse bands are concentric around CL-euhedral cores. If the ghost bands were quartz growth events happening during recrystallization, this would require that all of the grain boundaries migrated concentrically outwards for adjacent crystals, which is impossible because a grain boundary can only advance at the expense of a neighboring crystal.

**5.5.6. CL-Chaotic Texture in Low Temperature Main Stage Quartz.** CL-mottled textures are conspicuously absent from Main Stage veins imaged in this study and by Rusk et al. [10]. The maximum temperature of formation of Main Stage veins is  $\sim 350^{\circ}\text{C}$  [15], so perhaps CL-mottled texture can only form during higher temperature recrystallization. The abundance of CL-chaotic texture in Main Stage quartz and its absence in pre-Main Stage quartz suggest that the mechanism of its formation is also a lower temperature process. It is plausible that CL-chaotic texture is formed by way of fast growth as sucrosic quartz crystals ripened and impinged on one another. CL-chaotic texture bears a striking resemblance to the plumose quartz texture identified in epithermal deposits, commonly alongside colloform quartz. Both plumose quartz and colloform quartz are thought to form as chalcedony converts to quartz [65, 85, 86]. Further work is required to understand the formation of the CL-chaotic texture.

## 6. Conclusions

This contribution shows how vein quartz strain and recrystallization modify primary growth textures, including those in quartz stockworks that are characteristic of the bottoms of porphyry Cu deposits. We find that ductile deformation at lithostatic pressures is common at the base of the deposit, providing a potential constraint for better understanding of the architecture of dissected or more poorly understood porphyry systems. Recrystallized barren quartz and quartz-molybdenite veins record the conditions of deformation. Our findings show that Ti-in-quartz concentrations can provide meaningful estimates of quartz growth and deformation temperatures, but textural observations are key to accurate interpretation.

## Data Availability

The microprobe Ti measurements used to support the findings of this study are included within the supplementary information file, along with additional CL and hand sample images.

## Conflicts of Interest

The authors have no conflicts of interest to declare.

## Acknowledgments

This research was supported by the National Science Foundation grant no. EAR1524665. We thank John Dilles for thoughtful feedback. We are thankful to Montana Resources and the Washington Company for allowing access to the mine and samples. We are especially grateful to Steve Czehra and Amanda Griffith for their help, cooperation, and insight. Access to historic core was provided the Montana Bureau of Mines and Geology. We thank the staff of CAMCOR for their assistance with data collection, especially John Donovan and Julie Chouinard. We thank Kyle Eastmann for his assistance in sample acquisition. Mark Pearce was particularly helpful with respect to the presentation and interpretation of EBSD data and suggested we look into pipe diffusion. We thank Josephine Moore for her assistance with EBSD data collection.

## Supplementary Materials

The microprobe Ti data, additional CL images of Main Stage quartz, and hand sample images of stockwork vein textures can be found the Appendix. (*Supplementary Materials*)

## References

- [1] M. Reed, B. Rusk, and J. Palandri, “The Butte magmatic-hydrothermal system: one fluid yields all alteration and veins,” *Economic Geology*, vol. 108, no. 6, pp. 1379–1396, 2013.
- [2] C. W. Passchier and R. A. Trouw, *Microtectonics*, Springer Science & Business Media, 2005.
- [3] M. Stipp, H. Stünitz, R. Heilbronner, and S. M. Schmid, “The eastern Tonale fault zone: a ‘natural laboratory’ for crystal plastic deformation of quartz over a temperature range from 250 to 700 C,” *Journal of Structural Geology*, vol. 24, no. 12, pp. 1861–1884, 2002.
- [4] M. Stipp, H. Stünitz, R. Heilbronner, and S. M. Schmid, “Dynamic recrystallization of quartz: correlation between natural and experimental conditions,” *Geological Society, London, Special Publications*, vol. 200, no. 1, pp. 171–190, 2002.
- [5] M. Reed and J. Dilles, “Ore deposits of Butte, Montana. Montana Bureau of Mines and Geology Special Publication 122: Geology of Montana,” *Special Topics*, vol. 2, 2020, <http://www.mbgm.mtech.edu/pubs/GeologyofMontana/>.
- [6] H. W. Smedes, *Regional Tectonic Setting of the Boulder Batholith, (abs) in Guidebook for the Butte field Meeting of the Society of Economic Geologists: Butte, Society of Economic Geology, Montana*, 1973.
- [7] R. I. Tilling, “Composition and time relations of plutonic and associated volcanic rocks, Boulder batholith region, Montana,” *Bulletin of the Geological Society of America*, vol. 85, no. 12, pp. 1925–1930, 1974.
- [8] B. Rusk and M. Reed, “Scanning electron microscope–cathodoluminescence analysis of quartz reveals complex growth histories in veins from the Butte porphyry copper deposit, Montana,” *Geology*, vol. 30, no. 8, pp. 727–730, 2002.

- [9] B. G. Rusk, M. H. Reed, J. H. Dilles, and A. J. Kent, "Intensity of quartz cathodoluminescence and trace-element content in quartz from the porphyry copper deposit at Butte, Montana," *American Mineralogist*, vol. 91, no. 8-9, pp. 1300–1312, 2006.
- [10] B. Rusk, H. Lowers, and M. Reed, "Trace elements in hydrothermal quartz: relationships to cathodoluminescent textures and insights into vein formation," *Geology*, vol. 36, no. 7, pp. 547–550, 2008.
- [11] E. A. Du Bray, J. N. Aleinikoff, and K. Lund, *Synthesis of Petrographic, Geochemical, and Isotopic Data for the Boulder Batholith, Southwest Montana*, US Department of the Interior, US Geological Survey, 2012.
- [12] B. Berger, T. Hildenbrand, and J. O'Neill, *Control of Precambrian Basement Deformation Zones on Emplacement of Laramide Boulder Batholith and Butte Mining District, Montana, United States*, US Department of the Interior, US Geological Survey, 2011.
- [13] S. A. Roberts, *Early hydrothermal alteration and mineralization in the Butte district, Montana*, [Ph.D. thesis], Harvard University, 1975.
- [14] R. I. Tilling, M. R. Klepper, and J. D. Obradovich, "K-Ar ages and time span of emplacement of the Boulder batholith, Montana," *American Journal of Science*, vol. 266, no. 8, pp. 671–689, 1968.
- [15] B. G. Rusk, M. H. Reed, and J. H. Dilles, "Fluid inclusion evidence for magmatic-hydrothermal fluid evolution in the porphyry copper-molybdenum deposit at Butte, Montana," *Economic Geology*, vol. 103, no. 2, pp. 307–334, 2008.
- [16] R. A. Houston and J. H. Dilles, "Structural geologic evolution of the Butte district, Montana," *Economic Geology*, vol. 108, no. 6, pp. 1397–1424, 2013.
- [17] R. H. Sillitoe and J. W. Hedenquist, "Linkages between volcanotectonic settings, ore-fluid compositions, and epithermal precious metal deposits," *Society of Economic Geologists Special Publication*, vol. 10, pp. 315–343, 2003.
- [18] M. T. Einaudi, J. W. Hedenquist, and E. Esra Inan, "Sulfidation state of fluids in active and extinct hydrothermal systems: transitions from porphyry to epithermal environments," *Special Publication-Society of Economic Geologists*, vol. 10, pp. 285–314, 2003.
- [19] C. A. Heinrich, "The physical and chemical evolution of low-salinity magmatic fluids at the porphyry to epithermal transition: a thermodynamic study," *Mineralium Deposita*, vol. 39, no. 8, pp. 864–889, 2005.
- [20] C. Pudack, W. Halter, C. A. Heinrich, and T. Pettke, "Evolution of magmatic vapor to gold-rich epithermal liquid: the porphyry to epithermal transition at Nevados de Famatina, Northwest Argentina," *Economic Geology*, vol. 104, no. 4, pp. 449–477, 2009.
- [21] L. Maydagán, M. Franchini, B. Rusk et al., "Porphyry to epithermal transition in the Altar Cu-(Au-Mo) deposit, Argentina, studied by cathodoluminescence, LA-ICP-MS, and fluid inclusion analysis," *Economic Geology*, vol. 110, no. 4, pp. 889–923, 2015.
- [22] C. Meyer, "An early potassic type of wall-rock alteration at Butte, Montana," *American Mineralogist: Journal of Earth and Planetary Materials*, vol. 50, pp. 1717–1722, 1965.
- [23] G. H. Brimhall, *Mineralogy, Texture, and Chemistry of Early Wall Rock Alteration in the Deep Underground Mines and Continental Area, Butte District, Montana*, Society of Economic Geologists, 1973.
- [24] R. H. Sillitoe, "Porphyry copper systems," *Economic Geology*, vol. 105, no. 1, pp. 3–41, 2010.
- [25] A. Müller, R. Herrington, R. Armstrong et al., "Trace elements and cathodoluminescence of quartz in stockwork veins of Mongolian porphyry-style deposits," *Mineralium Deposita*, vol. 45, no. 7, pp. 707–727, 2010.
- [26] D. A. Wark and E. B. Watson, "TitaniQ: a titanium-in-quartz geothermometer," *Contributions to Mineralogy and Petrology*, vol. 152, no. 6, pp. 743–754, 2006.
- [27] R. Huang and A. Audétat, "The titanium-in-quartz (TitaniQ) thermobarometer: a critical examination and re-calibration," *Geochimica et Cosmochimica Acta*, vol. 84, pp. 75–89, 2012.
- [28] M. D. Acosta, J. M. Watkins, M. H. Reed, J. J. Donovan, and D. J. DePaolo, "Ti-in-quartz: evaluating the role of kinetics in high temperature crystal growth experiments," *Geochimica et Cosmochimica Acta*, vol. 281, pp. 149–167, 2020.
- [29] F. Bachmann, R. Hielscher, and H. Schaeben, "Texture analysis with MTEX-free and open source software toolbox," in *Solid State Phenomena*, pp. 63–68, Trans Tech Publications Ltd, 2010.
- [30] J. J. Donovan, J. W. Singer, and J. T. Armstrong, "A new EPMA method for fast trace element analysis in simple matrices," *American Mineralogist*, vol. 101, no. 8, pp. 1839–1853, 2016.
- [31] J. L. Urai, W. D. Means, and G. S. Lister, "Dynamic recrystallization of minerals," in *Mineral and Rock Deformation: Laboratory Studies*, , , 1986161 - 199, 1986.
- [32] G. Lambrecht and L. W. Diamond, "Morphological ripening of fluid inclusions and coupled zone-refining in quartz crystals revealed by cathodoluminescence imaging: implications for CL-petrography, fluid inclusion analysis and trace-element geothermometry," *Geochimica et Cosmochimica Acta*, vol. 141, pp. 381–406, 2014.
- [33] R. S. Nelson, D. J. Mazey, and R. S. Barnes, "The thermal equilibrium shape and size of holes in solids," *Philosophical Magazine*, vol. 11, no. 109, pp. 91–111, 1965.
- [34] E. Roedder, "Fluid inclusions," in *Reviews in Mineralogy*, vol. 12, pp. 1–644, Mineralogical Society of America, 1984.
- [35] A. Tarantola, L. W. Diamond, and H. Stünitz, "Modification of fluid inclusions in quartz by deviatoric stress I: experimentally induced changes in inclusion shapes and microstructures," *Contributions to Mineralogy and Petrology*, vol. 160, no. 6, pp. 825–843, 2010.
- [36] C. W. Field, L. Zhang, J. H. Dilles, R. O. Rye, and M. H. Reed, "Sulfur and oxygen isotopic record in sulfate and sulfide minerals of early, deep, pre-Main Stage porphyry Cu-Mo and late Main Stage base-metal mineral deposits, Butte district, Montana," *Chemical Geology*, vol. 215, no. 1-4, pp. 61–93, 2005.
- [37] C. N. Mercer and M. H. Reed, "Porphyry Cu-Mo stockwork formation by dynamic, transient hydrothermal pulses: mineralogic insights from the deposit at Butte, Montana," *Economic Geology*, vol. 108, no. 6, pp. 1347–1377, 2013.
- [38] G. Zulauf, "Structural style, deformation mechanisms and paleodifferential stress along an exposed crustal section: constraints on the rheology of quartzofeldspathic rocks at supra- and infrastructural levels (Bohemian Massif)," *Tectonophysics*, vol. 332, no. 1-2, pp. 211–237, 2001.
- [39] S. Piazolo, D. J. Prior, and M. D. Holness, "The use of combined cathodoluminescence and EBSD analysis: a case study investigating grain boundary migration mechanisms in quartz," *Journal of Microscopy*, vol. 217, no. 2, pp. 152–161, 2005.

- [40] M. W. Jessell, E. Siebert, P. D. Bons, L. Evans, and S. Piazolo, "A new type of numerical experiment on the spatial and temporal patterns of localization of deformation in a material with a coupling of grain size and rheology," *Earth and Planetary Science Letters*, vol. 239, no. 3-4, pp. 309–326, 2005.
- [41] R. Gardner, S. Piazolo, L. Evans, and N. Daczko, "Patterns of strain localization in heterogeneous, polycrystalline rocks—a numerical perspective," *Earth and Planetary Science Letters*, vol. 463, pp. 253–265, 2017.
- [42] A. Halfpenny, D. J. Prior, and J. Wheeler, "Analysis of dynamic recrystallization and nucleation in a quartzite mylonite," *Tectonophysics*, vol. 427, no. 1-4, pp. 3–14, 2006.
- [43] R. H. Wightman, D. J. Prior, and T. A. Little, "Quartz veins deformed by diffusion creep-accommodated grain boundary sliding during a transient, high strain-rate event in the Southern Alps, New Zealand," *Journal of Structural Geology*, vol. 28, no. 5, pp. 902–918, 2006.
- [44] B. P. Kashyap, A. Arieli, and A. K. Mukherjee, "Microstructural aspects of superplasticity," *Journal of Materials Science*, vol. 20, no. 8, pp. 2661–2686, 1985.
- [45] M. Bestmann and D. J. Prior, "Intragranular dynamic recrystallization in naturally deformed calcite marble: diffusion accommodated grain boundary sliding as a result of subgrain rotation recrystallization," *Journal of Structural Geology*, vol. 25, no. 10, pp. 1597–1613, 2003.
- [46] Z. Jiang, D. J. Prior, and J. Wheeler, "Albite crystallographic preferred orientation and grain misorientation distribution in a low-grade mylonite: implications for granular flow," *Journal of Structural Geology*, vol. 22, no. 11-12, pp. 1663–1674, 2000.
- [47] S. White, "Geological significance of recovery and recrystallization processes in quartz," *Tectonophysics*, vol. 39, no. 1-3, pp. 143–170, 1977.
- [48] L. F. Morales, G. E. Lloyd, and D. Mainprice, "Fabric transitions in quartz via viscoplastic self-consistent modeling part I: axial compression and simple shear under constant strain," *Tectonophysics*, vol. 636, pp. 52–69, 2014.
- [49] D. Mainprice, J. L. Bouchez, P. Blumenfeld, and J. M. Tubià, "Dominant c slip in naturally deformed quartz: implications for dramatic plastic softening at high temperature," *Geology*, vol. 14, no. 10, pp. 819–822, 1986.
- [50] G. S. Lister and U. F. Dornsiepen, "Fabric transitions in the Saxony granulite terrain," *Journal of Structural Geology*, vol. 4, no. 1, pp. 81–92, 1982.
- [51] U. Nakaya, "The deformation of single crystals of ice," *IAHS Publications*, vol. 47, pp. 229–240, 1958.
- [52] H. R. Wenk, N. Barton, M. Bortolotti et al., "Dauphiné twinning and texture memory in polycrystalline quartz. Part 3: texture memory during phase transformation," *Physics and Chemistry of Minerals*, vol. 36, no. 10, pp. 567–583, 2009.
- [53] M. Sintubin and H. R. Wenk, "Dauphiné twins or not, that's the question," in *EGU General Assembly Conference Abstracts*, p. 1935, Vienna, Austria, 2014.
- [54] R. Asada, N. Shimobayashi, and M. Kitamura, "Equilibrium form of negative crystals in igneous quartz," *Journal of Mineralogical and Petrological Sciences*, vol. 97, no. 2, pp. 59–69, 2002.
- [55] A. H. Shen, W. A. Bassett, and I. M. Chou, "The  $\alpha$ - $\beta$  quartz transition at high temperatures and pressures in a diamond-anvil cell by laser interferometry," *American Mineralogist*, vol. 78, no. 7-8, pp. 694–698, 1993.
- [56] N. H. Gray, "Geometric selection in two-dimensional crystal aggregates," *Journal of the International Association for Mathematical Geology*, vol. 16, no. 1, pp. 91–100, 1984.
- [57] S. Nollet, C. Hilgers, and J. L. Urai, "Experimental study of polycrystal growth from an advecting supersaturated fluid in a model fracture," *Geofluids*, vol. 6, no. 2, 2006.
- [58] I. Sunagawa, *Crystals: Growth, Morphology, & Perfection*, Cambridge University Press, 2007.
- [59] F. Wendler, A. Okamoto, and P. Blum, "Phase-field modeling of epitaxial growth of polycrystalline quartz veins in hydrothermal experiments," *Geofluids*, vol. 16, no. 2, 2016.
- [60] A. Okamoto and K. Sekine, "Textures of syntectonic quartz veins synthesized by hydrothermal experiments," *Journal of Structural Geology*, vol. 33, no. 12, pp. 1764–1775, 2011.
- [61] V. I. Rakin, "Morphotypes of the quartz basic rhombohedra and crystallization conditions," *Crystallography Reports*, vol. 62, no. 4, pp. 511–521, 2017.
- [62] C. J. L. Wilson, "Crystal growth during a single-stage opening event and its implications for syntectonic veins," *Journal of Structural Geology*, vol. 16, no. 9, pp. 1283–1296, 1994.
- [63] E. Ukar, S. E. Laubach, and R. Marrett, "Quartz c-axis orientation patterns in fracture cement as a measure of fracture opening rate and a validation tool for fracture pattern models," *Geosphere*, vol. 12, no. 2, pp. 400–438, 2016.
- [64] R. Fournier, "The behavior of silica in hydrothermal solutions," *Review in Economic Geology*, vol. 2, pp. 45–60, 1985.
- [65] T. Shimizu, "Reinterpretation of quartz textures in terms of hydrothermal fluid evolution at the Koryu Au-Ag deposit, Japan," *Economic Geology*, vol. 109, no. 7, pp. 2051–2065, 2014.
- [66] D. J. Cherniak, E. B. Watson, and D. A. Wark, "Ti diffusion in quartz," *Chemical Geology*, vol. 236, no. 1-2, pp. 65–74, 2007.
- [67] M. C. Jollands, E. Bloch, and O. Muntemer, "New Ti-in-quartz diffusivities reconcile natural Ti zoning with time scales and temperatures of upper crustal magma reservoirs," *Geology*, vol. 48, no. 7, pp. 654–657, 2020.
- [68] A. M. Van den Kerkhof, A. Kronz, K. Simon, and T. Scherer, "Fluid-controlled quartz recovery in granulite as revealed by cathodoluminescence and trace element analysis (Bamble sector, Norway)," *Contributions to Mineralogy and Petrology*, vol. 146, no. 5, pp. 637–652, 2004.
- [69] G. D. Bromiley and M. Hiscock, "Grain boundary diffusion of titanium in polycrystalline quartz and its implications for titanium in quartz (TitaniQ) geothermobarometry," *Geochimica et Cosmochimica Acta*, vol. 178, pp. 281–290, 2016.
- [70] W. O. Nachlas and G. Hirth, "Experimental constraints on the role of dynamic recrystallization on resetting the Ti-in-quartz thermobarometer," *Journal of Geophysical Research: Solid Earth*, vol. 120, no. 12, pp. 8120–8137, 2015.
- [71] M. Bestmann, G. Pennacchioni, B. Grasemann, B. Huet, M. W. Jones, and C. M. Kewish, "Influence of deformation and fluids on Ti exchange in natural quartz," *Journal of Geophysical Research: Solid Earth*, vol. 126, no. 12, 2021.
- [72] D. Grujic, M. Stipp, and J. L. Wooden, "Thermometry of quartz mylonites: importance of dynamic recrystallization on Ti-in-quartz reequilibration," *Geochemistry, Geophysics, Geosystems*, vol. 12, no. 6, 2011.
- [73] M. Haertel, M. Herwigh, and T. Pettke, "Titanium-in-quartz thermometry on synkinematic quartz veins in a retrograde crustal-scale normal fault zone," *Tectonophysics*, vol. 608, pp. 468–481, 2013.

- [74] M. Bystricky, K. Kunze, L. Burlini, and J. P. Burg, "High shear strain of olivine aggregates: rheological and seismic consequences," *Science*, vol. 290, no. 5496, pp. 1564–1567, 2000.
- [75] V. G. Toy, D. J. Prior, and R. J. Norris, "Quartz fabrics in the Alpine Fault mylonites: influence of pre-existing preferred orientations on fabric development during progressive uplift," *Journal of Structural Geology*, vol. 30, no. 5, pp. 602–621, 2008.
- [76] Y. Boneh, L. F. Morales, E. Kaminski, and P. Skemer, "Modeling olivine CPO evolution with complex deformation histories: implications for the interpretation of seismic anisotropy in the mantle," *Geochemistry, Geophysics, Geosystems*, vol. 16, no. 10, pp. 3436–3455, 2015.
- [77] C. Pu and Y. Gao, "Crystal plasticity analysis of stress partitioning mechanisms and their microstructural dependence in advanced steels," *Journal of Applied Mechanics*, vol. 82, no. 3, 2015.
- [78] C. J. Wilson, "Experimental work on the effect of pre-existing anisotropy on fabric development in glaciers," *Geological Society, London, Special Publications*, vol. 176, no. 1, pp. 97–113, 2000.
- [79] P. J. Hudleston, "Structures and fabrics in glacial ice: a review," *Journal of Structural Geology*, vol. 81, pp. 1–27, 2015.
- [80] B. A. Marmo and C. J. Wilson, "The stress distribution related to the boudinage of a visco-elastic material: examples from a polar outlet glacier," *Geological Society, London, Special Publications*, vol. 176, no. 1, pp. 115–134, 2000.
- [81] J. Skarmeta, "Structural controls on alteration stages at the Chuquicamata copper-molybdenum deposit, Northern Chile," *Economic Geology*, vol. 116, no. 1, pp. 1–28, 2021.
- [82] S. Piazolo, A. La Fontaine, P. Trimby et al., "Deformation-induced trace element redistribution in zircon revealed using atom probe tomography," *Nature Communications*, vol. 7, no. 1, pp. 1–7, 2016.
- [83] S. M. Reddy, N. E. Timms, P. Trimby, P. D. Kinny, C. Buchan, and K. Blake, "Crystal-plastic deformation of zircon: a defect in the assumption of chemical robustness," *Geology*, vol. 34, no. 4, pp. 257–260, 2006.
- [84] M. B. Holness and G. R. Watt, "Quartz recrystallization and fluid flow during contact metamorphism: a cathodoluminescence study," *Geofluids*, vol. 1, no. 3, 2001.
- [85] M. V. Sander and J. E. Black, "Crystallization and recrystallization of growth-zoned vein quartz crystals from epithermal systems; implications for fluid inclusion studies," *Economic Geology*, vol. 83, no. 5, pp. 1052–1060, 1988.
- [86] J. R. Vearncombe, "Quartz vein morphology and implications for formation depth and classification of Archaean gold-vein deposits," *Ore Geology Reviews*, vol. 8, no. 5, pp. 407–424, 1993.